CRUSHING PROPERTIES OF HEXAGONAL ADHESIVELY BONDED HONEYCOMBS LOADED IN THEIR TUBULAR DIRECTION

A thesis
Presented to
The Academic Faculty

By

Benoît Favre

In Partial Fulfillment
Of the Requirements of the Degree
Master of Science in Civil Engineering

Georgia Institute of Technology

March, 2007

CRUSHING PROPERTIES OF HEXAGONAL ADHESIVELY BONDED HONEYCOMBS LOADED IN THEIR TUBULAR DIRECTION

Approved by:

Dr Mulalo Doyoyo, advisor
School of Civil and
Environmental Engineering
Georgia Institute of Technology

Dr Reginald Desroches, advisor
School of Civil and
Environmental Engineering
Georgia Institute of Technology

Dr Laurence J. Jacobs
School of Civil and
Environmental Engineering
Georgia Institute of Technology

TABLE OF CONTENTS

Acknowledgement

I would like to thank all the people who made this project possible. The first one is of course Dr Doyoyo, my advisor, who supported me all along, and reviewed the parts of this thesis multiple times. I would also like to thank Dr Desroches for his help, in particular financial, which was a major reason for me to get involved in this project. Then I would like to thank two companies which were extremely helpful in the process of doing the testing, Hexcel Corp. who provided us with free honeycomb samples, and Correlated Solutions, who helped me get some results with the cameras in very short notice. Finally I want to thank all my friends who made these two years in Atlanta a good time.

List of figures

Summary

Aluminum hexagonal honeycombs loaded in their tubular direction have extremely good mechanical properties, including high stiffness to weight and energy absorption capacities. The corresponding load-displacement curve exhibits a long plateau accompanied by small fluctuations. These fluctuations are due to the propagation of a folding front through the studied sample, which is due to the creation of folds. This plateau load makes honeycombs the perfect candidates for use as energy-dissipative devices such as bumpers. Previous studies have largely focused on the study of the plateau load with less attention given to the length of the folds. However, it will be seen that this parameter is crucial for both the complete understanding of the mechanics of the folding and the derivation of the plateau load. We present first an introduction to the thematic of honeycomb. Then, the first model focuses precisely on the fold length. Two hypotheses are considered, a correlation between elastic buckling and folding first and a local propagation of the existing fold secondly. The second hypothesis is found to be correct, and the results are good for thin foils. For thick foils, a geometric limitation occurs, which makes the results less precise. Then, we are able to use the previous kinematics for the folding and derive a new set of formulas for the plateau load. The results are compared with experimental results and past formulas, and are found to be good, especially for thin foils, where our results for the fold length are more precise.

Keywords: cellular materials, metallic hexagonal honeycombs, plate theory, folding front wavelength, energy absorption, crushing distance.

1. Introduction

1.1 General presentation of metallic adhesively-joined honeycombs

Metallic honeycombs, and more generally honeycombs, are one of the most efficient light-weight structures used to dissipate energy. They combine high stiffness-to-weight properties with a crushing load plateau which makes them desirable for a very large range of applications, including transportation, aeronautics, and sandwiches structures where honeycomb gives its rigidity to the structure. However, their main drawback remains their high prices. For example the automobile industry uses simple non-connected steel tubes in their crash-box rather than honeycomb, although honeycomb would be more efficient in this purpose. Indeed the improvement of the properties brought by the use of honeycomb do not balance the higher cost induced for this type of applications. Therefore honeycomb remains an expensive and “high-tech” solution even our days. Probably its most common use is nowadays for sandwiches of small thicknesses, where honeycomb can give a high rigidity and are not too much expensive.

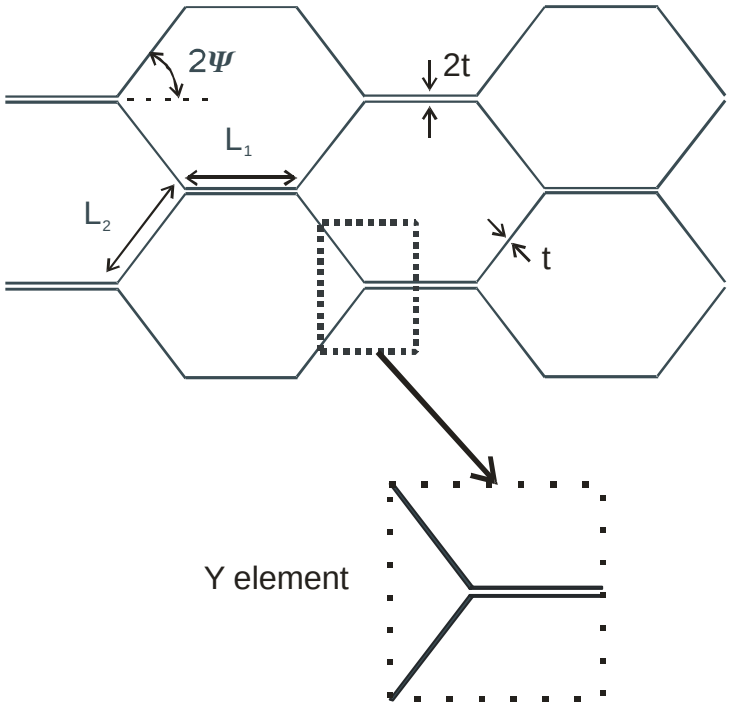

Fig. 1.1: Presentation of honeycomb, viewed in its tubular direction.

The purpose of this thesis is to study the crushing properties of a particular type of honeycomb, namely adhesively-bonded honeycomb. This type of honeycomb is made by extruding, adhesively bonding, and expanding multiple plates typically composed of aluminum or mild steel. The final structure is very similar to a space filling combination of tubes as figured in Fig. 1.1. It must be noted that the study presented in this thesis is only valid for adhesively bonded honeycombs; brazed honeycombs for instance would possess different properties which are not studied here. The aim of this study is to characterize the crushing properties of honeycomb when loaded in its tubular direction. A test setup is described in the following. A typical force/displacement curve is exhibited in Fig. 1.2. The curve is composed of an elastic part which ends when the first fold appears, which characterize the peak load. After this peak, honeycombs exhibit a very interesting force plateau with small fluctuations. Physically, the plateau is due to the creation of folds that propagate throughout the sample while the crushing advances. The first fold appears either at the top or at the bottom of the sample. Then, the sample is divided into two parts, a crushed part and an uncrushed or intact part. The folding front progresses from the top of the sample –if the first fold has appeared here– to the bottom, while folds appear one close to the other. When the front has reached the end opposite to the one where it started (if it started at the top, when he reaches the bottom), then folds are created in the whole sample. Since it is not anymore possible to create folds, the rigidity of the structure raises abruptly, which we name densification. We will use in the following the configuration of the tests (where a sample is axially crushed by a vertical actuator) as the reference: “vertical” will refer to the tubular direction, while “horizontal” refers to the two directions perpendicular to the tubular direction.

Additionally we introduce here the concept of Y element: the Y element, which was introduced in Fig. 1.1, is the smallest repetitive pattern to recreate the structure. It can be seen in Fig. 1 that this pattern is made of two plates adhesively joined.

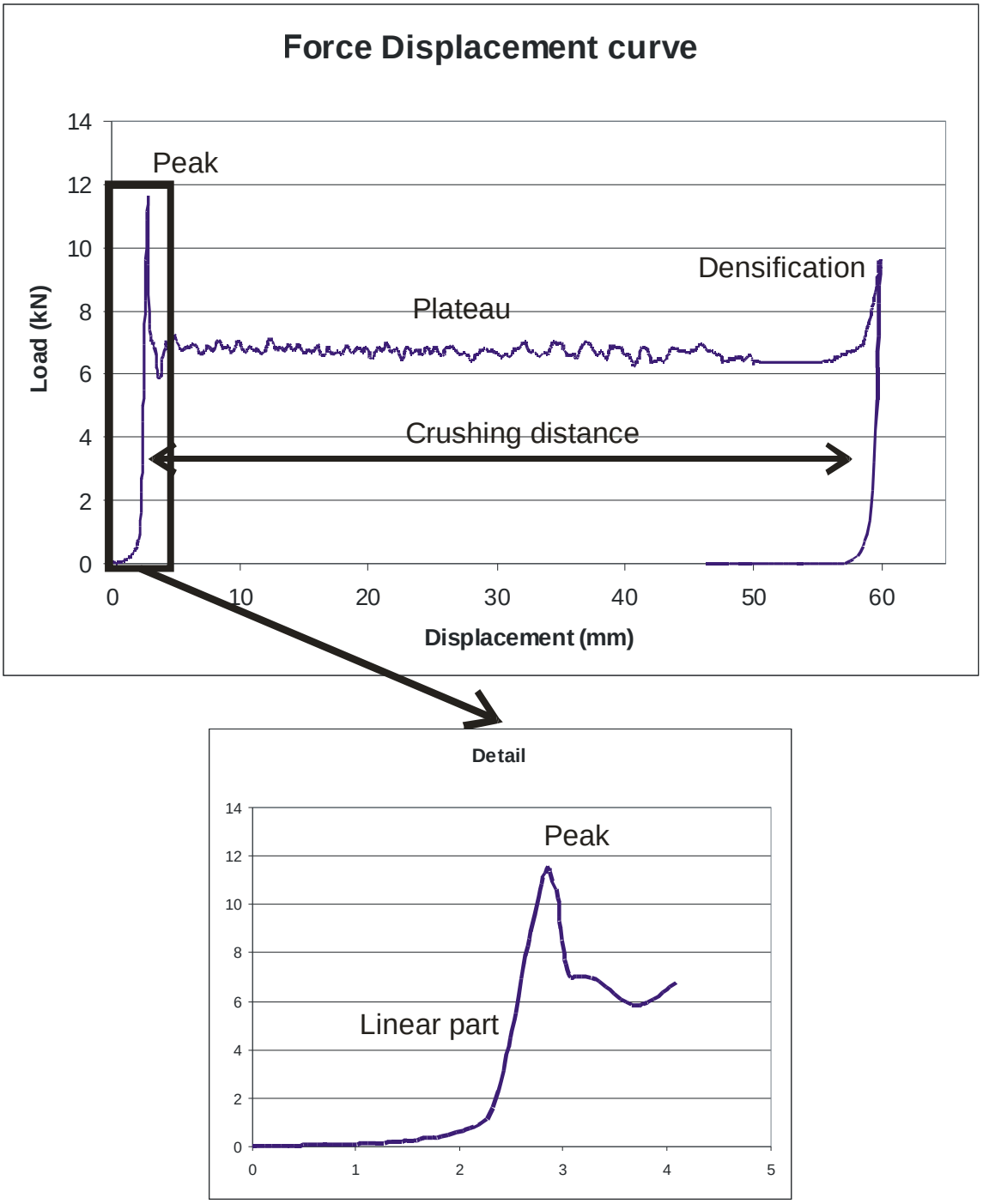

Fig. 1.2: Typical force/displacement curve for the axial crushing of adhesively-bonded honeycomb.

1.2 Literature review

The literature is abundant on the topic of honeycomb. It will be shown that the material has been studied in all configurations and strains rates, which means that its applications cover a broad range. However, the crushing of hexagonal honeycombs in their tubular direction, which is the concern of most applications, is still not understood.

Let us first introduce some more background information. Honeycombs are part of a more general type of materials which are porous structures. These structures can be two dimensional (in which case they are called honeycombs) or three dimensional (and they are called foams). The main advantage is that this type of structures is a lot lighter than the original material they are built from. The drawback is that the properties of the resultant material are not as good as the original material. However, for certain configurations, the stiffness can be still high (in particular for honeycombs), and the final material is highly crushable, while the original material is not. Honeycombs, which are two-dimensional structures, present indeed a very high stiffness in their tubular direction compared to their weight. This property was the property used for the first historical applications of honeycombs, namely aeronautics (wings of planes, notably for the American bomber B36) and spatial applications. The first studies of honeycombs focused logically on the elastic properties of honeycombs loaded in their tubular direction (Kelsey (1958)). The development of honeycombs with more stable crushing properties allowed in the 60s and 70s the use of honeycombs as crushable protective cushions. Their main use as crushable material nowadays is as bumpers in car-crash testing. This new ability was first studied by Mc Farland (1963), who focused on the folding pattern of hexagonal honeycombs loaded in their tubular direction. The first deep study of the mechanisms included in the folding pattern is due to Wierzbicki (1983) twenty years later. In his paper, Wierzbicki refines the work of Mc Farland on axially loaded hexagonal honeycombs, introduce new kinematics and conclude with simple formulas for the crushing strength and the fold length. However, his derivation of the fold length is based on principles that are mechanically not correct; the kinematics field is not coherent; and it will be seen that its model lacks of a few ideas like how the folding front propagates through the sample. These are the reason why we started this work. Later the work of Gibson and Ashby (1988) gives relatively good results for the same problem, but does

not study the core of the problem, i.e. the precise kinematics at the micro-structural level. Lately a few papers have been released on axially crushed metallic hexagonal honeycombs. The most interesting one is from Mohr and Doyoyo (2003). Using conservation equations (of mass, energy…) as in fluid mechanics they characterize the folding front's progression in the material while it is continuously crushed. However they avoid this way to study the micro-structural crushing kinematics. I also appreciate a paper from Aminanda et Castagnie (2005), whose approach consists in considering only the junction between the three plates of a *Y*-element. It will be seen that our model, in which a very large part of the total dissipated energy is dissipated in this junction, can explain very well their result. However, I totally disagree with the idea of springs for the implementation in finite element codes, as proposed by the authors of this paper, and would rather prefer an energy approach rather easy to encode.

In the meanwhile, the increasing use of honeycomb as crash barriers has required scientists to study other aspects of its crushing. In particular shear and the effect of high strain-rates have been studied extensively, as well as the in-plane properties. These aspects are not the focus of this study, we will only give a few references here.

The problem of the behavior of honeycombs in shear is easier than the compression. It was studied by Gibson and Ashby (1988) by energy methods, later by Grediac (1993) by finite elements, Hohe et all (1999) using homogenization or Qiao and Wang (2005) combining the different techniques. Some experimental papers should also be cited, see for example Doyoyo and Mohr (2003) for a nowadays classical setup for the shear tests. For the type of applications requiring a good resistance in shear, as well as the high speed ones, usually square honeycombs are preferred to hexagonal ones. See for example Cote et all (2005) for an experimental and finite element study of this aspect.

In-plane properties are weak compared to the tubular direction properties (two orders of magnitude of difference for the stiffness for example). However, some authors have studied that in detail (although I wonder which applications they aim at). The most famous is from Papka and Kiriakides (1994), it uses finite elements extensively to predict the behavior of hexagonal honeycombs loaded in one of their in-plane directions (the strongest one).

Finally, the effect of strain rates on any of the previous types of loading has been studied. The best study is due to Xue and Hutchinson (2005), where the authors use a finite element simulation to propose a continuous medium model for the dynamic crushing of square honeycomb loaded in their tubular direction. Some other papers, like the one of McShane et all (2005) are also interesting. In this paper the authors compare the blast properties of square honeycombs compared to the plain aluminum plate of same mass as the honeycomb tested. The honeycomb is found to behave better than the aluminum plate, making it a candidate for the protection for blast. There are a multitude of papers on the combination of loads, strain rates, using one of the classical methods (finite elements and experiments for most of the papers, but also homogenization and analysis for the bravest) but they are not the scope of this study so I will stop here. However, it must be pointed that of all these papers, the closest to solving the problem of the crushing of hexagonal honeycombs loaded in their tubular direction is Wierzbicki's one, which has the limitation we noted before. And this problem remains the heart of the behavior of hexagonal honeycombs and their main application. Therefore, this study is plainly justified.

1.3 Prospects of this study

The prospect of this study is to characterize the complete crushing of hexagonal honeycombs loaded in their tubular direction. Remember Fig. 1.2. We start with the elastic regime by computing the elastic buckling pattern and comparing with the peak stress. Then, we need to characterize the crushing plateau. The previous studies have focused on the crushing stress, however it appears that another parameter is important, namely the fold length. It needs to be determined to really understand the crushing mechanics, and it is very easy to compute another interesting parameter to define the energy absorption of a sample, namely the crushing distance, from the fold length. The crushing distance is intuitive and can be observed directly from Fig. 1.2: it is the difference between the original height of the sample and its height when fully crushed. For these two reasons (deeper understanding and derivation of the crushing distance) the first part of our study is focused on this parameter. The results are found to be good for thin foils, which are the most useful honeycombs for energy application purposes. Completing this first study allows us to fully determine the kinematics of the folding

process. Then, we are able to study the crushing strength using the results from the fold length. The results are found to be very good for thin foils, where we had good results for the fold length. For thick foils, the results are better than previous results from past studies, but the errors tend to be much larger than for thin foils. Some explanations on the reasons for this are given.

2. Experiments

The aluminum honeycomb investigated in this study was manufactured by Hexcel Corporation. The specific samples studied were composed of aluminum alloy 5052, with (1) cell size 3/16 in. (4.76 mm), mass density 3.1 pcf (49.66 kg/m3) and foil thickness 0.001 in. (2.54e-2 mm); (2) cell size 5/32 (3.97 mm), mass density 2.6 pcf (41.65 kg/m3) and foil thickness 0.0007 in. (1.78e-2 mm). Three tests each were conducted for the above two different materials specifications. The dimensions of the specimens were 146×120×70 mm. Note that the latter dimension corresponds to the tubular direction. The samples were placed between two parallel wood plates strengthened with thin aluminum plates and compressed along the tubular direction with a custom-designed testing machine (Instron 8802, 2×50 kN load cells in the vertical direction). See Fig. 2.1 for an example of un-deformed and deformed photographs of the honeycomb sample. The experiments were performed under displacement-controlled conditions with a slow loading rate of 3 mm/min. The displacement and the resulting load acting on the sample were recorded in the Instron-provided data acquisition system. The force-displacement curve has already been presented in Fig. 1.2.

Additionally, we used a non-contact deformation measurement method to get the deformation of the walls of the sample. This method uses two cameras in correlation working like two eyes, meaning that from two images taken from close positions an integrated software computes the displacement field in the three directions (the two directions perpendicular to the focal axis directly, the third direction by correlating the two images). Figure 2.2 presents an elastic buckling pattern illustrating the way all the results were obtained from the cameras. The software always computes the displacement field on the whole area of interest. It is then possible to extract data along a given curve or line. All the displacement fields obtained in the following sections come from this method. The whole crushing process was monitored using two cameras configured in correlation as seen in Fig. 2.2 (1392x1040, monochrome, Schneider Optics Xenoplan 1.4/23mm Compact Series Lenses, distance 114 mm, frame rate 0.5 fps).

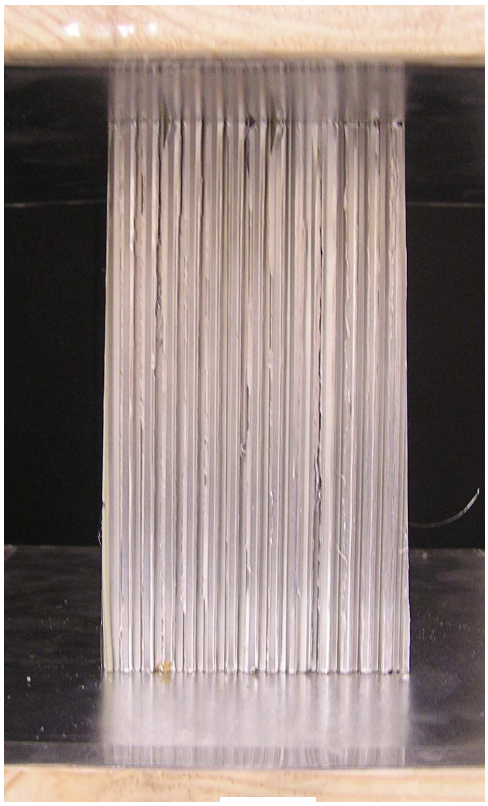

(a)

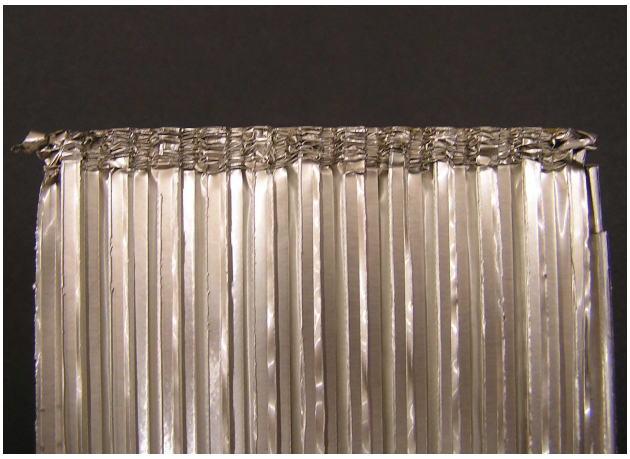

(b)

Fig. 2.1: Photos of the crushing experiment. Figure 2.1 (a) presents the initial setting before the load is applied, while Fig. 2.1 (b) presents the sample partially crushed. The crushed part, the intact part, as well as the crushing front, can be easily visualized.

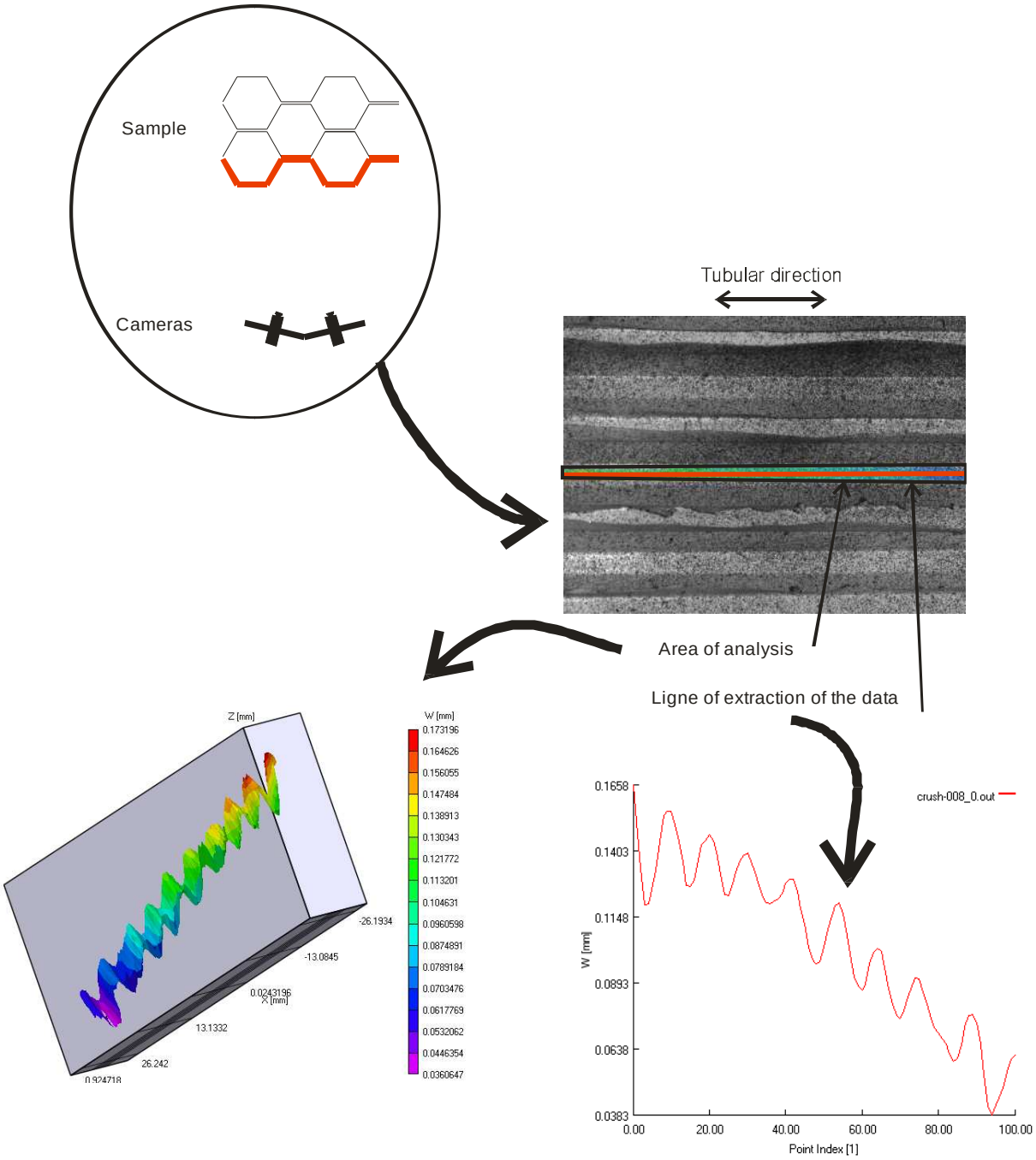

Fig. 2.2: Extraction of the data using cameras in correlation. It is possible to view the displacement in the whole area of interest and therefore to extract the relevant data along a given line of the space.

3. Phenomenology

This section is devoted essentially to the understanding of the different stages of the crushing of honeycomb, as exhibited in Fig. 1.2. As the honeycomb is continuously crushed, the Euler buckling point of the plates is reached. As seen in Fig. 2.2, the buckling pattern is characterized by a “sea” of out-of-plane elastic buckles. Once the elastic buckles appear, the stiffness of the honeycomb structure decreases with increasing displacement until the peak force is reached. Before the peak point, some hinge lines appear which prefigure the formation of the first fold. The increase in force induces the creation of what civil engineers call a mechanism, allowing large deformations and the apparition of the first fold. From this study it will be seen that the hinge lines accommodate large deformations and dissipate the elastic bending energy responsible for the buckling pattern while initiating the folding process.

We start the description of the folding pattern by presenting Wierzbicki’s view of the folding process, which can be found in Fig. 3.1. It must be stressed out that Wierzbicki’s analysis, as well as ours, is based on the idea of the propagation of a crushing front throughout the material while it is crushed. The crushing front splits the sample into two parts, an uncrushed, intact part and a folded part, and all the deformation in the sample is localized in the crushing front. The folding process is characterized by the combination of a vertical displacement of the top edges (line $A_1F_1D_1$), inducing a horizontal displacement of the hinge line $A_2F_2D_2$. Indeed, the angle ψ remains constant during the transformation, which requires $A_2F_2D_2$ moving horizontally (out of its original plane). Therefore, the surfaces $A_1F_1F_2A_2$ and $A_2F_2F_3A_3$, which were four rectangles at the beginning of the folding process, are transformed into four trapezoids. Note that the surface $D_1F_1F_2D_2$, which was bonded by adhesive between two different plates, shows some partial delamination.

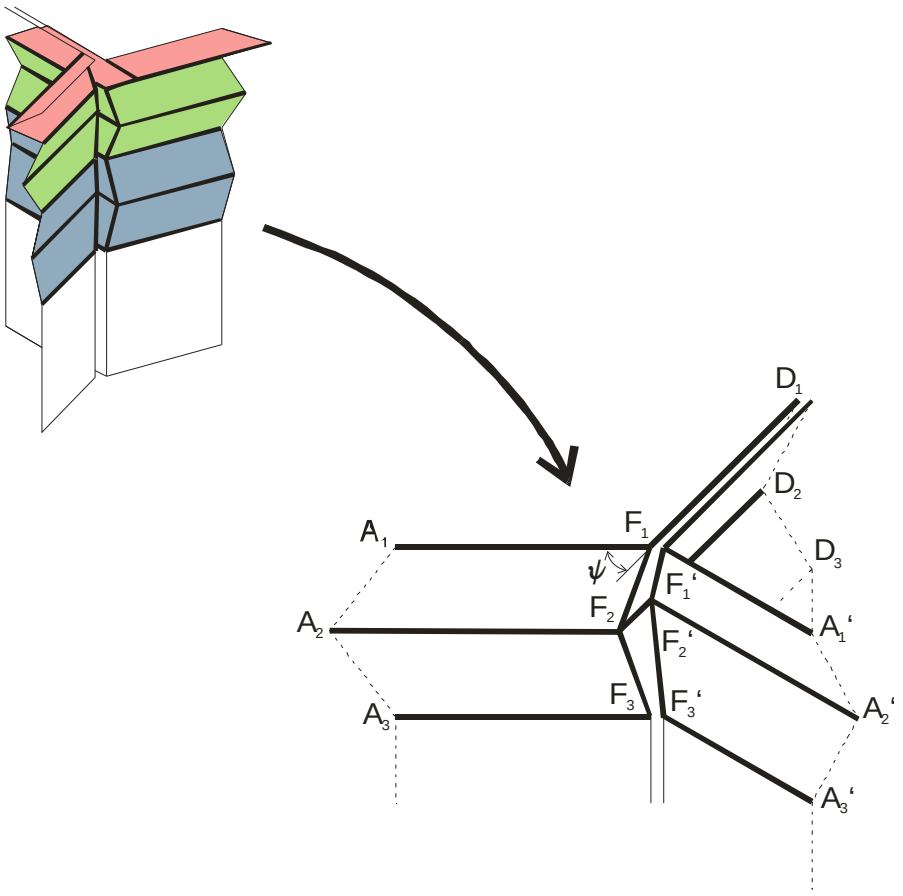

Fig. 3.1: Folding front in Wierzbicki's work. The thick lines represent hinge lines, the dashed one are just the boundaries of the studied part. The notation *H* will be used in the whole paper with the same meaning.

The latter presentation has the great advantage of giving a lot of good ideas about the folding mechanism: the necessary combination of horizontal and vertical displacement for the hinge lines of the crushing front, as well as partial delamination of the bonded plates. However, it misses a critical part of the phenomenon, namely the dynamics of the propagation. We develop in this section a model which has all these characteristics, derived from Wierzbicki's one. The main defect of Wierzbicki's model is that it analyses each fold alone and does not account for the interaction between the active fold and the nucleating fold. A major issue in the analysis is to understand that folds can potentially form in two different ways (see Fig. 3.2). If the folds are alternated, as figured in Fig. 3.3, then the solution is more energy efficient, because the hinge lines $A_1F_1D_1$ and $A_3F_3D_3$ are no longer necessary. The understanding of the hinge line is

radically modified from this perspective. Indeed, the process is now dynamic: one fold induces the next and the folds propagate vertically albeit asymmetrically —the part of the material on one side of the fold (top in Fig. 3.3, which is the crushed region) is different from the part on the other side (bottom, intact region).

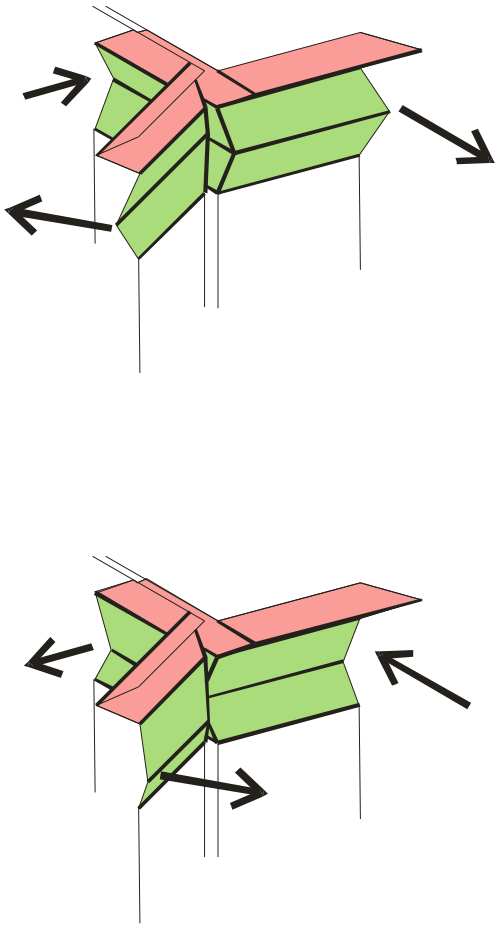

Fig. 3.2: Two ways of folding are possible. Again the thick lines represent hinge lines. The thin lines are not plastic, they are the boundaries of the representative element.

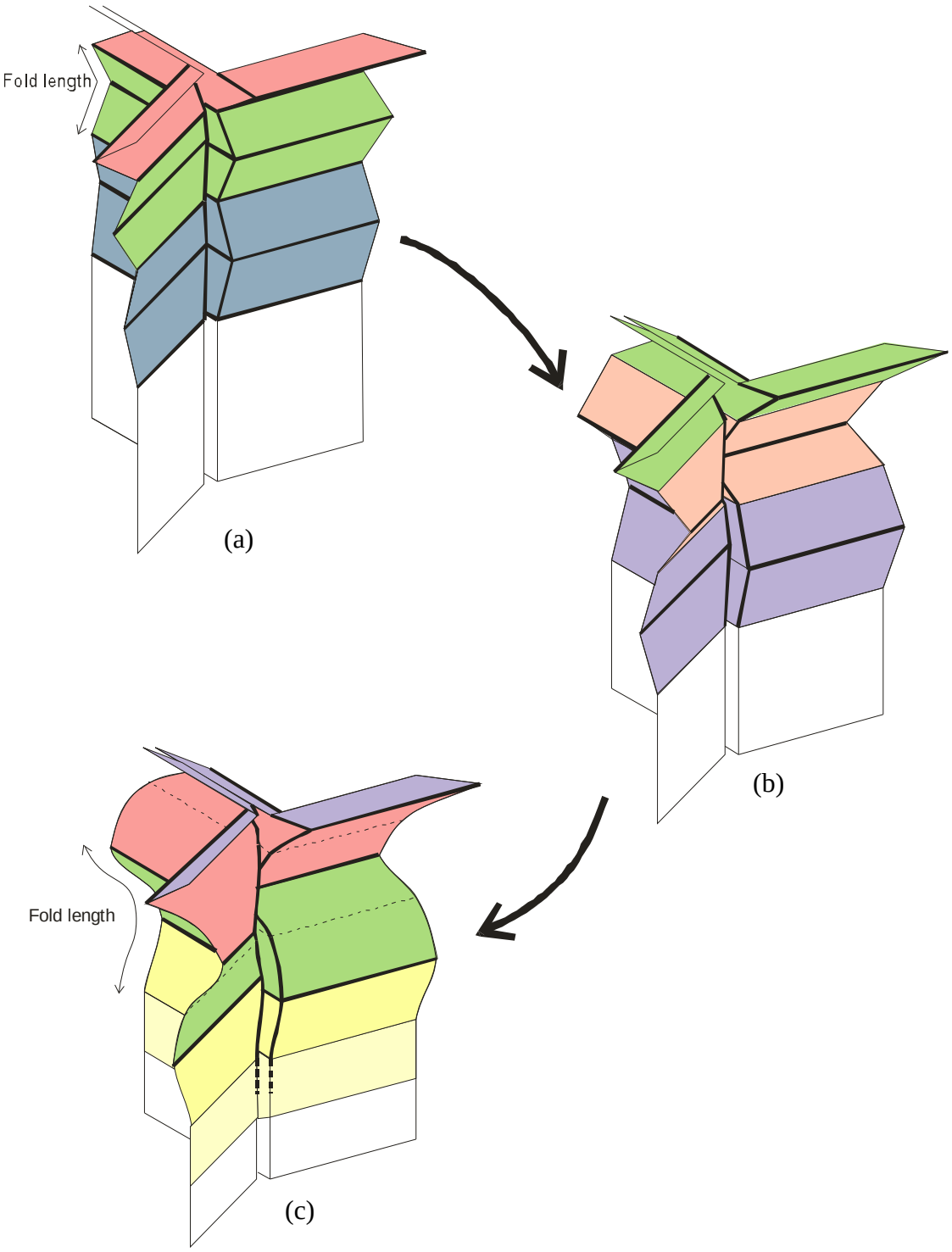

Fig. 3.3: Starting by Wierzbicki's model, we alternate the folds; then some hinge lines are no longer necessary and we obtain our model (c). Note that some hinge lines have disappeared in (c). The folding wavelength has been sketched too. Note that it is twice as large for (c) than for (a).

Another aspect of the propagation is the propagation in the horizontal direction (perpendicular to the tubular direction), which is equivalent to explain why the folds form a horizontal “fold front”. Figure 3.4 presents different top views (in the tubular direction) of the folding process, a possible case and an impossible one. It can be seen that the configuration of one fold in the horizontal plane influences the configurations of all its close neighbors. The reason for this is that one solution requires much less stretching energy from the double thickness plate than the other.

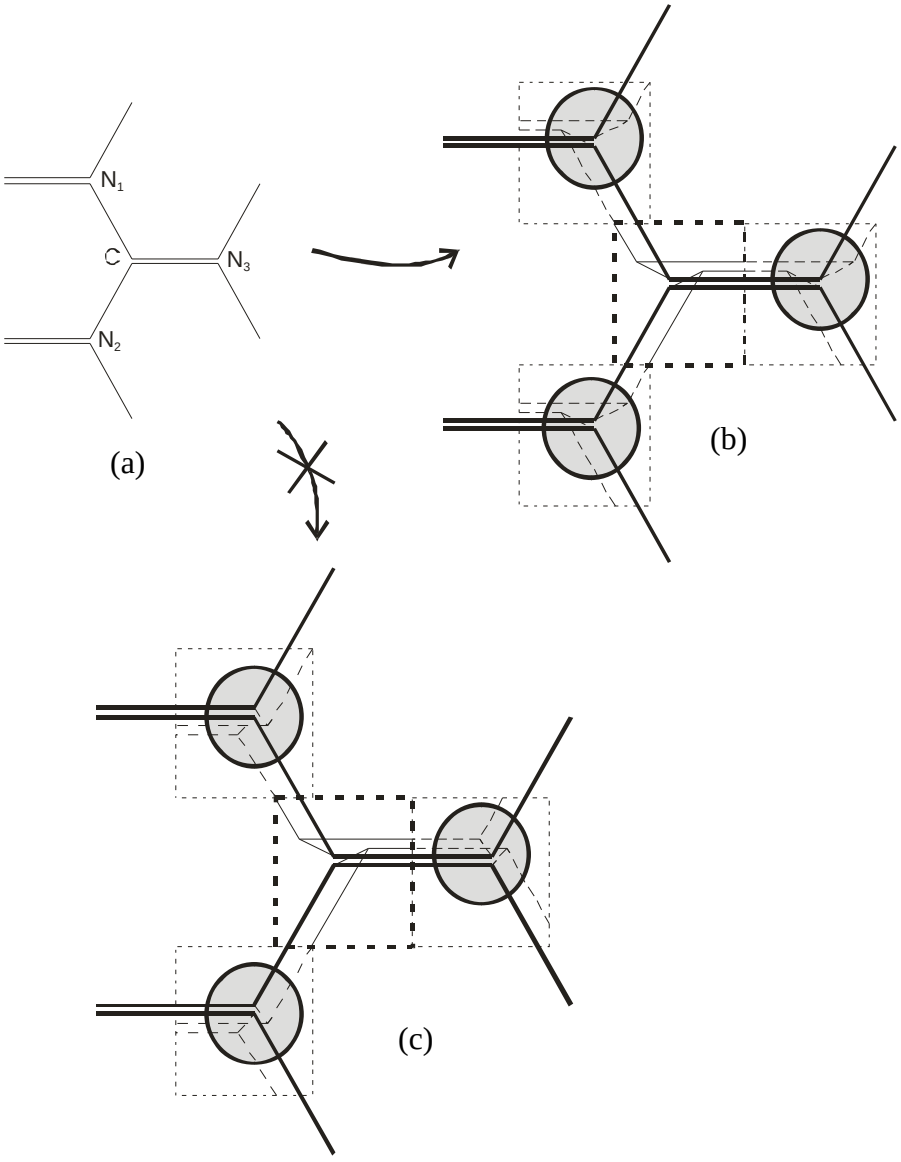

Figure 3.4: Propagation of the fold in the plane perpendicular to the tubular direction. Fig. 3.4 (b) is the correct folding mode, although Fig. 3.4 (c) shows an impossible mode due to high energies of stretching in the close junctions between the three plates of the *Y* elements.

4. Study of the fold length

4.1 Presentation

This part of this thesis is devoted to understanding the physical process behind the final folding length. Our first and intuitive guess was that the fold length is determined by the elastic part of the deformation, i.e. that the buckling pattern was directly responsible for the fold pattern. In this vision the fold length would have been the same as the length of the buckles in the buckling pattern. It can already be seen that the very local character of honeycomb folding does not seem to fit with this assumption. Indeed this condition would mean that the folds can appear all at the same time (since the buckling is associated to a buckling mode for the whole sample). However the propagation of the folds is very local, and it was found that the buckling pattern is not the factor originating the folds. Indeed, when the peak force is reached, which coincides with the creation of the first fold, the elastic bending energy of the buckling is dissipated in the plastic hinges composing the fold. Instead of large elastic deflections for the plates in the whole sample (the deflections due to buckling can be seen directly with human eyes), the deformation becomes localized in the crushing front. In the rest of the sample (uncrushed region) on the other side the deformations become very small (the fluctuations can no longer be seen).

From what was said above we present first a buckling analysis of the honeycomb structure, and this for two reasons: (1) it allows us to test the intuitive hypothesis as to whether buckling and folding patterns directly correlate, and (2) it allows us to characterize the elastic part of the stress strain curve. This hypothesis happens to be wrong, so that we had to develop a better understanding of the physics behind the folding pattern. This is done as a second step by modifying the boundary conditions of the analysis and considering folding as a local propagating phenomenon. However, it will be seen that the second type of models is limited by a geometrical limitation in the folding pattern. This geometric limit, which can be understood very easily, has been expressed here as a limit between thin foils and thick ones. For thin foils, the results from the second model predict the correct fold length. However, for thick foils, we were not able to predict exactly what happens and only proposed an upper bound for the fold length.

The study of the buckling is itself divided into three model, two models where only one plate is considered, and one model where the buckling of the total *Y* element is considered. On the contrary, the study of the propagation of localized hinge lines is based on a model with only one single plate.

For all models, we make extensive use of small-deformation thin plate theory assuming that there is no delamination between the two bonded plates. This is clearly a rational assumption for the buckling models, but it can be not so relevant for the second type of model. However we believe that the assumption is still fine because the deflections are not large except in the very close surroundings of the fold. In the analysis, we also neglect all the out-of-plane plate stresses (stress σ_{33} as well as the shear stresses σ_{13} and σ_{23}, their resultants and moments for the plates are neglected, where 3 is the direction of the thickness of the plate). We further neglect all displacements at the junction of the *Y*-element for the *Y*-element model.

4.2 Study of the elastic buckling

4.2.1 Simply supported case

We first derive the classical solution of the simply supported case, which is intuitive and gives a good understanding of the more complex solutions we derive in the following. The model is presented in Fig. 4.1. Let ω be the lateral deflection of the plate strip out of its plane, σ the applied in-plane stress, *x* the width direction and *y* the longest direction of the strip, and $D = E \cdot t^3 / 12 \cdot (1-\nu^2)$ the rigidity where E is the Young modulus of the material, ν the Poisson's ratio. The dimensions of the plate are Λ (height), *L* (width) and *t* (thickness). The equilibrium equation is given as:

$$\frac{\partial^4 \omega}{\partial x^4} + 2 \cdot \frac{\partial^4 \omega}{\partial x^2 \cdot \partial y^2} + \frac{\partial^4 \omega}{\partial y^4} = -\frac{\sigma \cdot t}{D} \cdot \frac{\partial^2 \omega}{\partial y^2} \qquad (4.2.1)$$

Assuming that $\omega = \omega_0 f(x) \sin(m\pi y / \Lambda)$, the equilibrium equation implies that we can write $f(x)$ as:

$$f(x) = A_1 \cdot \cosh(\alpha \cdot x) + A_2 \cdot \sinh(\alpha \cdot x) + A_3 \cdot \cos(\frac{\beta}{i} \cdot x) + A_4 \cdot \sin(\frac{\beta}{i} \cdot x) \qquad (4.2.2)$$

With $\begin{cases}\alpha \\ \beta\end{cases} = \frac{m \cdot \pi}{\Lambda}\sqrt{1 \pm \frac{\Lambda}{m \cdot \pi} \cdot \sqrt{\frac{\sigma \cdot t}{D}}}$ (4.2.3)

where $i^2 = -1$ (β is pure imaginary under classical conditions).

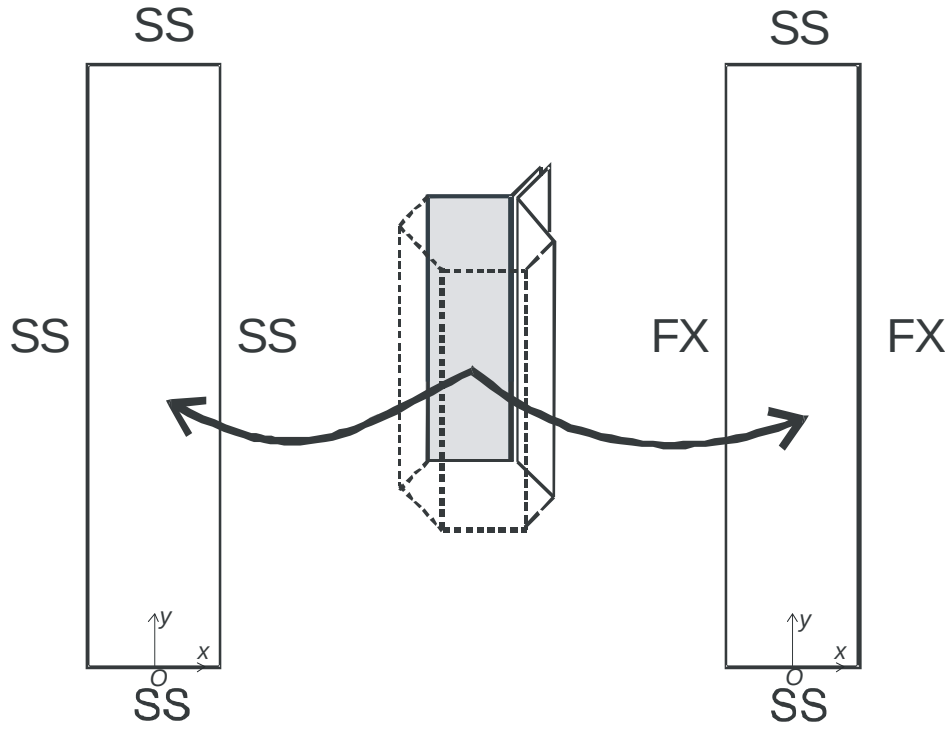

Fig. 4.1: Presentation of the simply-supported edges model (left), and fixed-edges model (right).

The boundary condition (plate simply supported) can be written for the vertical edges as $\omega(\pm L/2) = 0$ and $\left(\partial^2\omega/\partial x^2\right)(\pm L/2) = 0$. Hence, the conditions are already fulfilled by the edges $y = 0$ and $y = L$. From now on we introduce the notations $\alpha' = \alpha L/2$ and $\beta' = \beta L/2i$. Then the boundary conditions applied to the vertical edges can be written:

$$\begin{bmatrix} \cosh(\alpha') & -\sinh(\alpha') & \cos(\beta') & -\sin(\beta') \\ \cosh(\alpha') & \sinh(\alpha') & \cos(\beta') & \sin(\beta') \\ \alpha'^2\cosh(\alpha') & -\alpha'^2\sinh(\alpha') & \beta'^2\cos(\beta') & -\beta'^2\sin(\beta') \\ \alpha'^2\cosh(\alpha') & \alpha'^2\sinh(\alpha') & \beta'^2\cos(\beta') & \beta'^2\sin(\beta') \end{bmatrix} \begin{Bmatrix} A_1 \\ A_2 \\ A_3 \\ A_4 \end{Bmatrix} = \begin{Bmatrix} 0 \\ 0 \\ 0 \\ 0 \end{Bmatrix} \quad (4.2.4)$$

Taking the determinant of this gives the condition

$$-(\alpha'^2-\beta'^2)^2\cosh(\alpha')\sinh(\alpha')\cos(\beta')\sin(\beta')=0 \tag{4.2.5}$$

Which only non-trivial solutions are solutions of

$$\cos(\beta')\sin(\beta')=\sin(\beta')/2=0 \tag{4.2.6}$$

Introducing the parameters $K=\sigma t L^2/\pi^2 D$ (plate "stress") and $\phi=\Lambda/L$ we can write the previous equation as

$$g(K,\phi)=\sin\left(\frac{m\pi}{2\phi}\sqrt{\frac{\sqrt{K}}{m}\phi-1}\right)=0 \tag{4.2.7}$$

It is indeed an implicit equation between these 2 parameters, and *K* will have to be found for any given value of ϕ. However, here we can solve the implicit equation using the properties of the sin function and find the final condition

$$K=\frac{4n^2\phi}{m}+\frac{m}{\phi} \tag{4.2.8}$$

This plate stress represents the minimal stress to apply to a plate to see the buckling pattern appear. In terms of bifurcation it is the force at the point where the bifurcation begins.

The configuration is found to be $\omega=\omega_0\cos(n\pi x/L)\sin(m\pi y/\Lambda)$. If one computes the energy of that plate the total energy is found to be 0. This means that the configuration chosen is a local minimum of the energy; in fact it is the actual buckling mode. Therefore the parameter ω_0 can't be determined by a 1st order analysis. This explains why the authors choose to minimize the force here, considering that the lower force that will be reached will produce the corresponding mode shape.

Therefore we have to find the right combination of m and n in (4.2.8). Obviously we have to take $n=1$. The determination of m gives either $\text{int}(\phi^{-1})$ or $\text{int}(\phi^{-1})+1$. A simple analysis of the corresponding minimum shows that

$$\text{if } \phi^{-1} < \sqrt{\text{int}(\phi^{-1})(\text{int}(\phi^{-1})+1)} \text{ then } m=\text{int}(\phi^{-1}), \text{ else } m=\text{int}(\phi^{-1})+1 \qquad (4.2.9)$$

In consequence we can predict the number of small waves (buckles) appearing in the vertical direction.

4.2.2 Fixed vertical edges assumption

We assume now that the vertical edges are fixed (see Fig. 4.1). We don't need to assume that the horizontal edges are fixed too, because first they are very small compared to the vertical ones in our case; second we don't really know the boundary condition on these edges, it depends on the conditions of the experiment. The condition in Eq. (4) becomes for the fixed case $\omega(\pm L/2)=0$ and $\partial\omega/\partial x(\pm L/2)=0$. This gives the system:

$$\begin{bmatrix} \cosh(\alpha') & -\sinh(\alpha') & \cos(\beta') & -\sin(\beta') \\ \cosh(\alpha') & \sinh(\alpha') & \cos(\beta') & \sin(\beta') \\ -\alpha'\sinh(\alpha') & \alpha'\cosh(\alpha') & \beta'\sin(\beta') & \beta'\cos(\beta') \\ \alpha'\sinh(\alpha') & \alpha'\cosh(\alpha') & -\beta'\sin(\beta') & \beta'\cos(\beta') \end{bmatrix} \begin{Bmatrix} A_1 \\ A_2 \\ A_3 \\ A_4 \end{Bmatrix} = \begin{Bmatrix} 0 \\ 0 \\ 0 \\ 0 \end{Bmatrix} \qquad (4.2.10)$$

The system can be split into two sub-systems that correspond respectively to the symmetric and anti-symmetric solutions (by respect to the vertical axe). We choose to keep only the symmetric solution (lower energy) which gives $A_2 = A_4 = 0$.

We can again find an implicit equation of the same type as Eq. (4.2.5):

$$\cosh(\alpha')\beta'\sin(\beta') + \cos(\beta')\alpha'\sinh(\alpha') = 0 \qquad (4.2.11)$$

Which in terms of *K* and ϕ gives the analogous equation to (4.2.7):

$$g(K,\phi)=\sqrt{\frac{\frac{\sqrt{K}}{m}\phi-1}{\frac{\sqrt{K}}{m}\phi+1}}\tan\left(\frac{m\pi}{2\phi}\sqrt{\frac{\sqrt{K}}{m}\phi-1}\right)+\tanh\left(\frac{m\pi}{2\phi}\sqrt{\frac{\sqrt{K}}{m}\phi+1}\right)=0 \qquad (4.2.12)$$

Note that this equation has infinite number of solutions. We always pick the first positive solution, which would correspond to $n=1$ in the simply supported case. This solution is found for $m\pi/2\phi\sqrt{\sqrt{K}\phi/m-1}\in[\pi/2;\pi]$. Therefore, for a given value of ϕ, the equation can be solved and *K* is found. The main problem is the fact that we don't know what *m* is. The solution we chose consists of computing all the solutions *K* for growing values of *m* ($m=1,2,3\ldots$). Once we have computed *K* for all the acceptable values of *m* we just find the minimum of *K* on all the values of *m*.

The equation (4.2.12) can not be solved analytically so that we implemented it in Matlab by using a dichotomy algorithm. We made the choice of mapping the whole range of values of ϕ and then interpolate between our computed values. We could also have only solved for a given value of ϕ. The structure of the program is given in Fig. 4.2. Using the program, we can for a given value of ϕ find the corresponding value of *m* and the plate "stress" *K*. Therefore we are able to characterize the buckling solution of the fixed-edges plate.

Step 1: create a “map” of the studied space (m,ϕ)

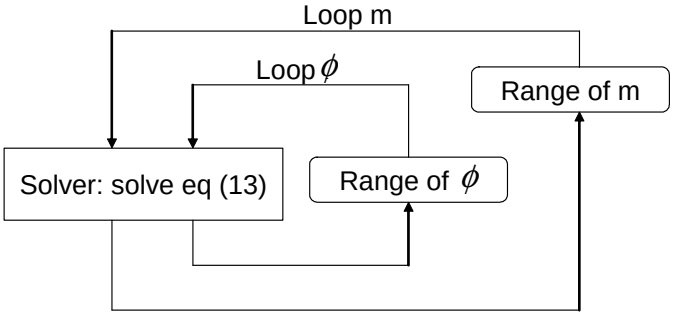

Step 2: extract the right data for a given ϕ

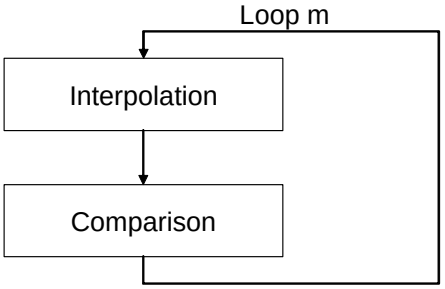

Fig. 4.2: Algorithm used in the study to find the value of *m* that gives the smallest value of *K*. We map the whole space (m, ϕ); then for a given value of ϕ we interpolate between the values computed before.

The final displacement can be written as:

$$\omega = \omega_0 \left(-\cos(\beta') \frac{\cosh(\alpha' \frac{2x}{L})}{\cosh(\alpha')} + \cos(\beta' \frac{2x}{L}) \right) \sin(\frac{m\pi y}{\Lambda}) \qquad (4.2.13)$$

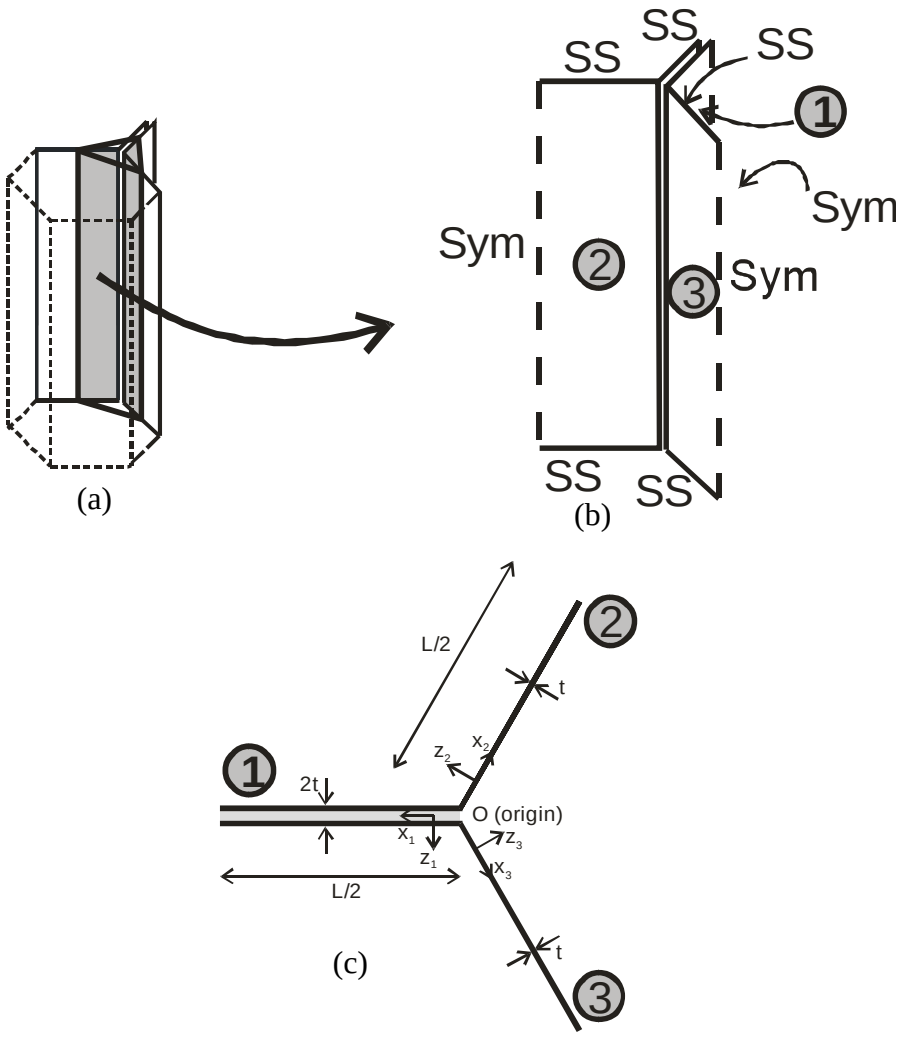

Fig. 4.3: Presentation of the *Y*-element model for the buckling analysis. The boundary conditions are given on (b) while the notations are given in (c). [ASIDE: SS stands for simply supported while Sym stands for Symmetry conditions.]

4.2.3 Study of the Y-element

The schematic of Fig. 4.3 presents the geometric quantities in the *Y*-element. Structurally, it is made of two plates bonded together on one of the side. In the following analysis, we will model it as three parts of plates bonded together at the junction of the *Y* element; two of them will have simple thickness *t*, while the bonded part will have thickness *2t*. For each plate the subscript *i* will be added to the corresponding quantities (deflection ω_i, rigidity of the plate D_i).

Consider that the displacement ω_i is given as a sine function for the vertical direction as follows:

$$\omega_i = \omega_0 f_i(x) \sin(\frac{m\pi y}{\Lambda}) \tag{4.2.14}$$

where *m* is an unknown parameter but common for the three plates, and $f_i(x)$ is an unknown function and different for each plate. The equilibrium equation (4.2.1) is valid for all three plates and gives the solution:

$$f_i(x) = A_{i1} \cdot \cosh(\alpha_i \cdot x + \gamma_i) + A_{i2} \cdot \sinh(\alpha \cdot x + \gamma_i) + A_{i3} \cdot \cos(\frac{\beta_i}{I} \cdot x + \gamma_i) + A_{i4} \cdot \sin(\frac{\beta_i}{I} \cdot x + \gamma_i) \tag{4.2.15}$$

The definition of α_i and β_i is identical as before except that the parameters *t* and *D* have to be adapted to the plate we are dealing with. This formulation is slightly more general than (4.2.2) because the phases γ_i have been added. In the particular case where the origin is taken at the middle of the plate (previous studies for simply supported or fixed edges) these phases are null, which explains why we did not have to introduce them before. However, here the origin is chosen to be the junction between the three plates, so that the phases have to be added.

We now have 12 coefficients A_{ij} which have to be evaluated using the boundary conditions. First we choose a symmetric solution for each plate, using the plane of symmetry $y = L/2$ (that is, the condition that $f_i(L/2 + x) = f_i(L/2 - x)$ for each plate). Therefore, we have the conditions

$$A_{i2} = A_{i4} = 0 \tag{4.2.16a}$$

$$\gamma_i = L/2 \tag{4.2.16b}$$

Using the notations $\alpha'_i = \alpha_i L/2$ and $\beta'_i = \beta_i L/2i$, we can now rewrite Eq. (4.2.15) as

$$f_i(x) = A_{i1} \cdot \cosh\left(\alpha'_i \cdot (\frac{2x}{L} - 1)\right) + A_{i2} \cdot \cos\left(\beta'_i \cdot (\frac{2x}{L} - 1)\right) \quad (4.2.17)$$

Note that there are now only six unknowns in our problem. We have to write the boundary conditions at the edge $x = 0$. These are $\omega(x = 0) = 0$ for all plates (no displacements at the junction), $\partial\omega/\partial x(0) = Cst$ for all plates (the rotation of the plates around the edge is constant), and $\sum M_x = 0$ (sum of moments around the vertical edge is zero). The moments M_x are computed as $M_x = -D\left(\left(\partial^2\omega/\partial x^2\right) - \nu\left(\partial^2\omega/\partial y^2\right)\right)$. The set of conditions can be written as a system of equations which have to simultaneously be verified. It is given in Annex. Again the condition is equivalent to equating the determinant of the system to zero. Introducing the variables $K = \sigma t L^2/\pi^2 D$ (simple thickness plate stress) and $\phi = \Lambda/L$ (ratio of the height of the sample to the cell size), we obtain an equation $g(K, \phi) = 0$ of the type of Eq. 4.2.7. Once again we find the minimum of *K* for a given value of ϕ, *m* being a parameter for the solution. The algorithm used is the same as before, except that the equation governing it is now the condition given by equating the determinant given in Annex 1 to zero.

It is also easy to show that for this solution the displacement is the same as Eq. 4.2.13.

4.2.4 Results and discussion

Figure 4.4 presents the number of folds computed for the three models as a function of the ratio ϕ. The result could be expected to be "pseudo-linear" since the equations of the type 4.2.7 were always functions of the ratio ϕ/m. The fact that it is a step function is due to the integer nature of *m*. The "linearity" coefficients are 1 for the simply supported case, 1.5 for the simply supported case, and 1.11 for the complete *Y*-element. This is completely rational, since the Y-element allows the transmission of moments at the junction, which can be seen as an average point between simply supported (no moments) and fixed edges (no rotations).

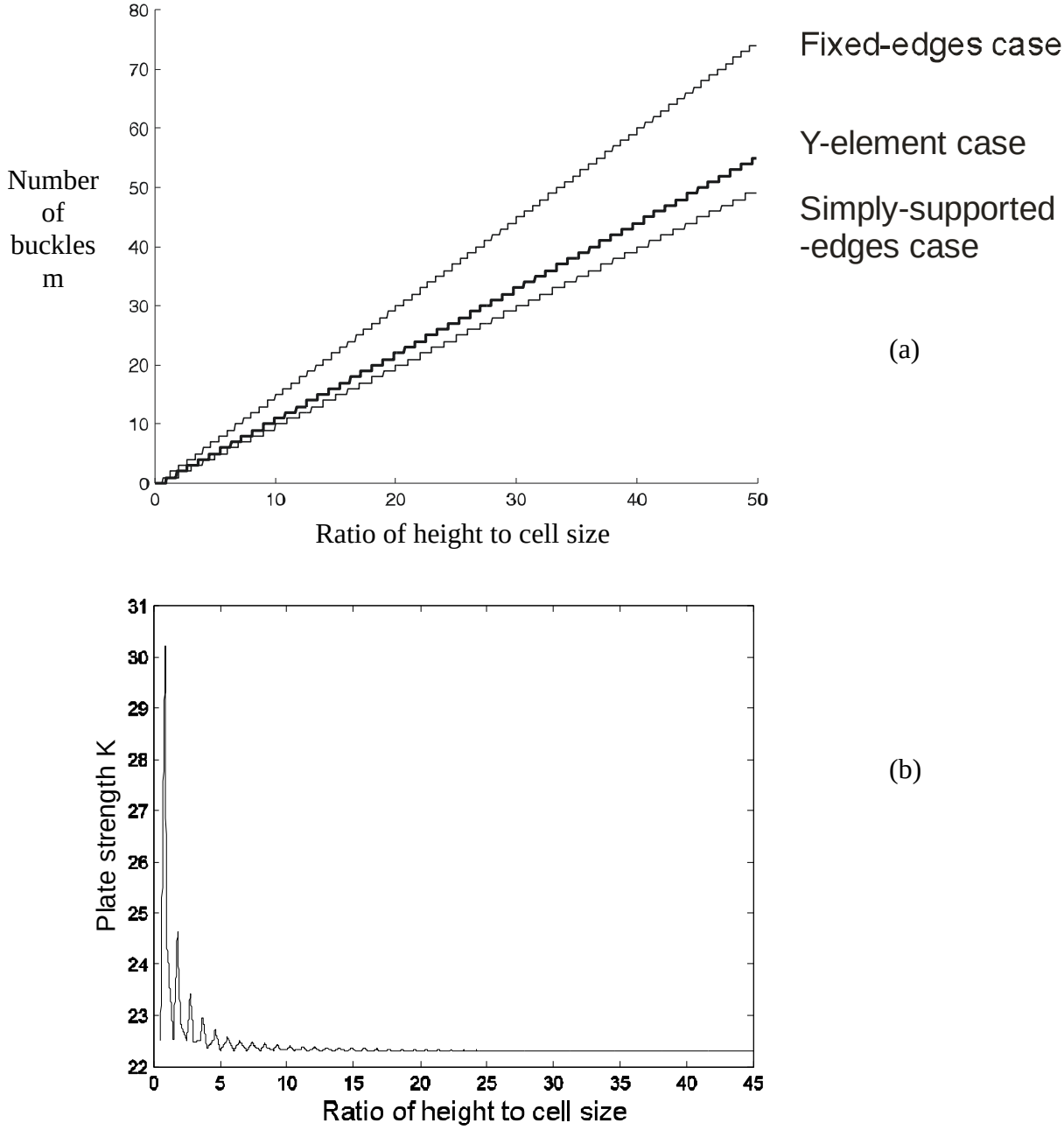

Fig. 4.4: Results of the buckling analysis: (a) presents m (number of buckles in the long direction of the plate) as a function of ϕ (ratio of long length of the plate on its small one) for the three cases studied (simply supported, fixed edges and *Y*-element) and (b) presents *K* (non-dimensional stress) as a function of ϕ, only for the *Y*-element study.

Although results were obtained for *K* as a function of ϕ, they are presented only for the *Y*-element. Indeed the simply supported case is given directly by Timoshenko

(1959) while the fixed case is relatively simple to compute. Additionally it does not bring any understanding to the model here. It can be seen that the final curve for K is the minimum of several curves for each value of m. From this second figure (Y-element case) we make the assumption that for $\phi > 3$ (which is fulfilled except for very thin layers of honeycomb) we can approach the rigidity by 22.5. Using the definition of K we can compute the minimal force needed to initiate the buckling of the structure. Then we can compare these results both with our experimental results and with Hexcel manual data. The comparison is given in Fig. 4.5. It can be seen that, as expected, the buckling starts before the peak stress of the material. The ratio between the peak stress and the buckling stress is not constant. It varies between 5% and 100%, with typical values around 15%. It tends to be larger for small thicknesses, and smaller for thicker samples. It can be seen that the difference between the buckling pattern and the apparition of the first hinge is however very noticeable, which most authors don't consider.

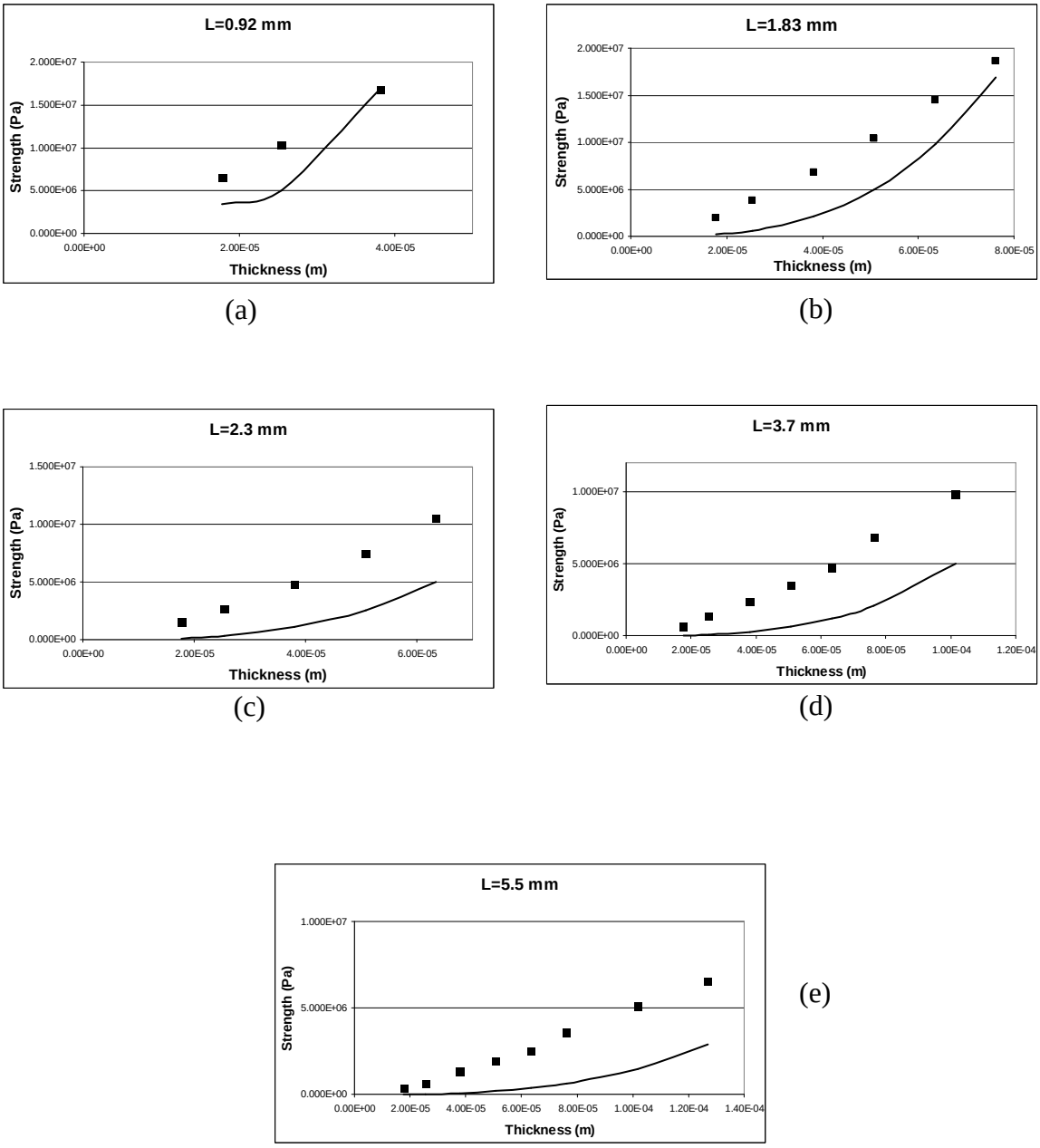

Fig. 4.5: Comparison of the minimum buckling stress computed here (solid line) and the peak stress given by the material supplier (Hexcel, squares). A good correlation is obtained.

We now want to explain the hypothesis stating that the buckling pattern and the folding pattern are directly correlated. For this we need to derive some additional results, including the displacement, stresses and hinges original positions. The displacements were already given as $\omega = \omega_0 \cos(n\pi x/L)\sin(m\pi y/\Lambda)$ (simply supported case) and Eq. 4.2.13 (fixed case and *Y*-element case). The resulting mode shapes for the simple case $\phi = 4$ are presented on fig. 4.6a and b for both the simply supported and the fixed edges cases. The mode shape for the *Y*-element has been said to be exactly similar to the fixed edges case, except that *m* is different, it is not presented here. It should be noted that:

- The number *m* is different for the different boundary conditions. For the simply supported case it is 4, although for the fixed edges case it is 7. The resulting mode shapes show a different number of waves.
- The boundary conditions are clearly different, the slope is null in the fixed edges case.

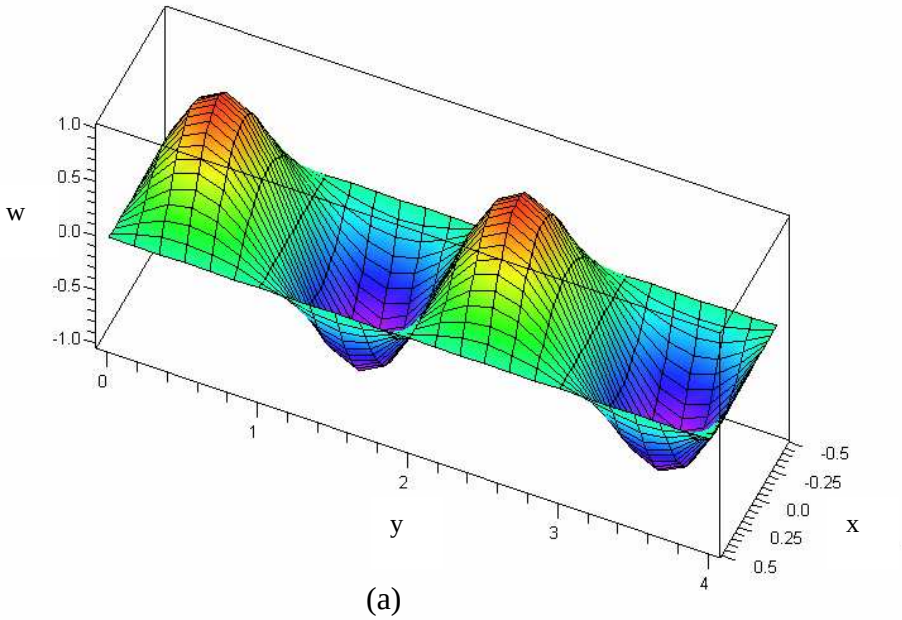

(a)

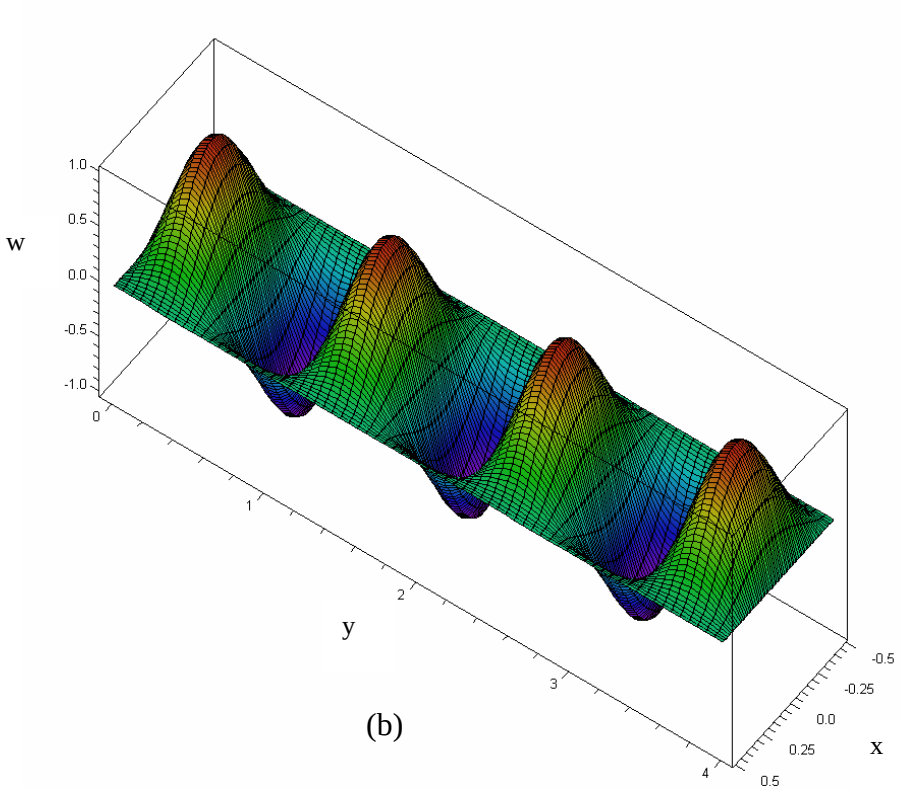

(b)

Fig. 4.6: Out-of-plane displacement for the simply supported case (a) and the fixed case (b).

The plate stresses can be found using Timoshenko (1959).

$$M_x = -D \cdot (\frac{\partial^2 \omega}{\partial x^2} + \nu \cdot \frac{\partial^2 \omega}{\partial y^2}) \quad M_y = -D \cdot (\nu \cdot \frac{\partial^2 \omega}{\partial x^2} + \frac{\partial^2 \omega}{\partial y^2}) \text{ and } M_{xy} = D \cdot (1-\nu) \cdot \frac{\partial^2 \omega}{\partial x \partial y} \qquad (4.2.18)$$

We use a yield criterion of the type of Von Mises:

$$c(N, M) = \frac{N^2}{t^2} + \frac{6^2 \cdot M^2}{t^4} \qquad (4.2.19)$$

Where in our case $N/t = \sigma$ is the axial force as computed before, and

$$M^2 = M_x^2 + M_y^2 - M_x \cdot M_y + 3 \cdot M_{xy}^2 \qquad (4.2.20)$$

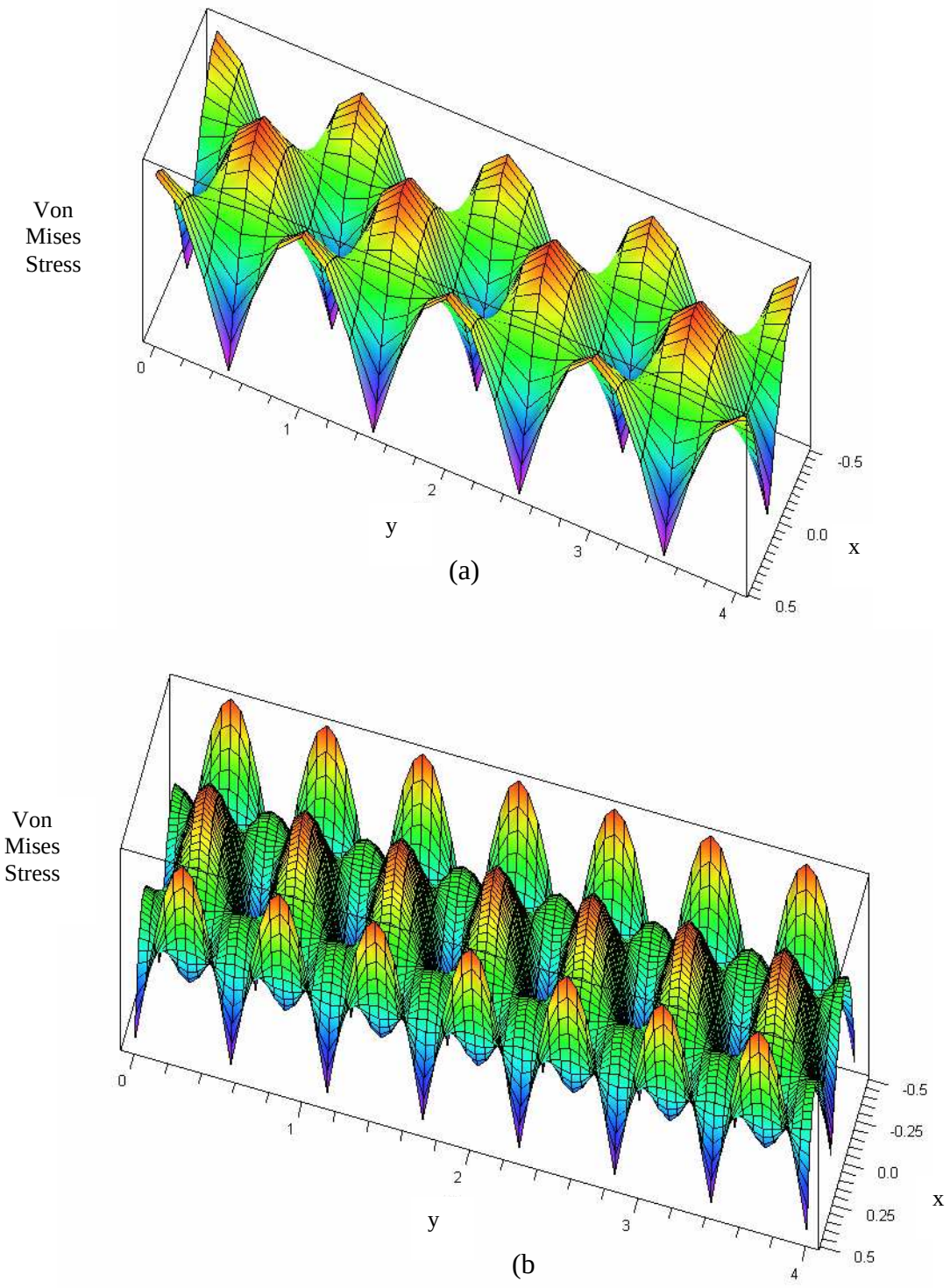

Fig. 4.7: Von Mised equivalent stress for the simply supported case (a) and the fixed case (b). The *Y*-element case shows the same pattern as (b) since the displacement is similar.

The state of stress can be computed and plotted. Since the in-plane stress is constant throughout the specimen we just plotted the moment part. Figure 4.7a and b present the state of stress (Von Mises equivalent stress) for the plate only simply supported and for the plate when the two vertical edges are fixed. Again the *Y*-element case is similar to the fixed edge case (the displacement of each plate of the model is exactly similar to the case where the conditions at its boundary would be fixed), so it was not plotted. It must be observed that the two figures are drastically different: indeed the number *m* is different, so that the number of waves is different. The other important thing to notice is the position of the peaks in the two cases. We focus on peaks on the boundary of the sample since there is a stress concentration here due to the combination of the three plates joined here. In the simply supported case, the peaks show a complicated pattern, they are not found at the same position *y* on the border and in the middle of the plate (they are found for the positions $y = k\,\Lambda/m$ with $k = 0.,1.\ldots m$ on the border); in the fixed case they are found for $y = (k+1/2)\,\Lambda/m$ with $k = 0.,1.\ldots m-1$, which corresponds exactly to the positions of the top of the waves. The perfect correlation between stress and strain allows us to make the hypothesis that the hinge lines appear at the positions of the peak displacements on the junction between the three plates. Then, there is a perfect correlation in this hypothesis between the buckling pattern and the folding pattern. The folding length, as defined in the next part, can be computed here as $\lambda_{buckling} = 4H$ with H given by $H = \Lambda / 2m = L / 2.22$. Therefore the folding length in this hypothesis becomes:

$$\lambda_{buckling} = L / 0.555 \qquad (4.2.20)$$

It must be noted that it does not depend on the specimen height, which is probably only true for specimens with a sufficiently large height.

4.3 Folding wavelength based on the propagation of localized plastic hinges

The observation as well as the quantitative results showed us that our intuition was in fact wrong. We had to develop a new model, which is presented in this part. We present first the experimental results that allowed us to get deeper understanding, to go as a second step to the modeling phase. The results are good for thin foils, which are our main focus.

4.3.1 Experimental observations

This part will include the results for honeycombs with very thin walls as well as those with thicker walls. Indeed the observation of the different samples during the experiments shows very different folding processes. Thus, different types of models are needed. The first case is the case of thin-walled honeycombs. The construction of the model is based on observations from image correlation given in Fig. 4.8. This figure presents the out-of-plane displacement of a stripe of material during the quasi-static crushing of the material. The lower limit of the analysis is the folded part of the honeycomb, since the cameras are unable to correlate regions of the material with very large strains and can not recognize planar areas. It must be pointed out before any further analysis that the elastic buckling pattern has totally disappeared from Fig. 4.8, while it induced large deformations before the appearance of the first fold (see Fig. 2.2). This is not an effect of scaling since the two scales are coherent. Therefore, the elastic energy stored as bending energy during the buckling pattern has been dissipated by the first fold. This means that the buckling pattern has little to no influence at all on the folding process and in particular on the folding wavelength. This result is rather non-intuitive; it will be checked numerically at the end of this section. Figure 4.8 shows that the folds seem to propagate according to the following process:

- The previous fold is closing up. This is characterized by an increase in the angles of rotation on both sides of the horizontal hinge line which creates the fold. This is accompanied with larger out-of-plane displacements at the position of the hinge line.
- As the out-of-plane displacements become large in the fold surroundings, they induce large stresses in the other parts of the plate. The plastic limit is reached

on the boundary and the stresses there produce an extension of the vertical hinge line along the junction between the plates (in the Y element).

- The stresses also reach the plastic limit in the middle of the plate, starting a new horizontal hinge line.
- Next, the force increases until the vertical hinge lines connect with the horizontal ones, allowing the folding mechanism to start.

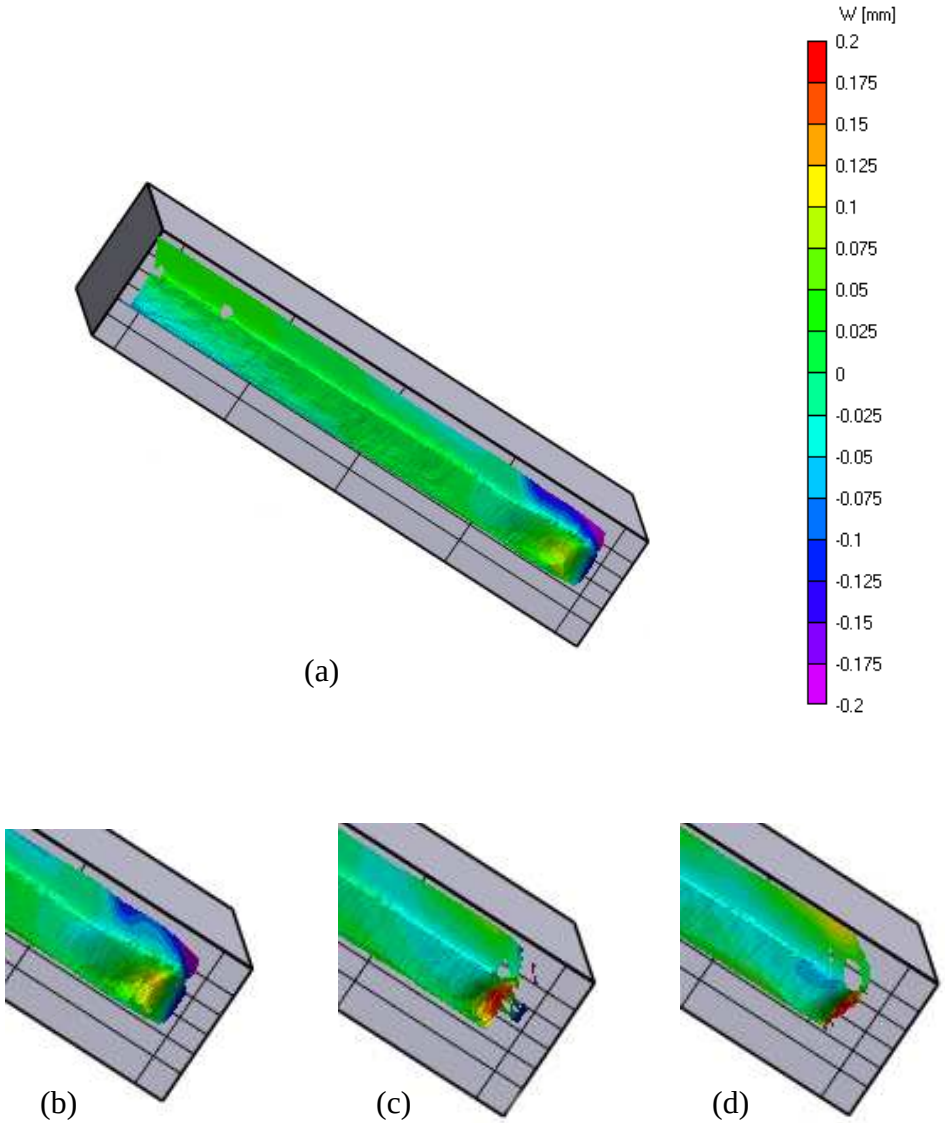

Fig. 4.8: Images obtained from the cameras illustrating the folding process. For all images *W* is the out-of-plane displacement using the same scale. They are ordered by increasing displacements. The right boundary disappears as the fold front progresses in the core of the sample.

Here, we briefly describe how we measure the folding wavelength. It is based on counting the number of folds in a completely crushed sample. We cut a very thin part of the honeycomb sample that is totally folded and stretch it by hand. The number of folds can then be counted very easily. As can be seen in Fig. 3.3, a fold comprises one horizontal hinge line like $A_2F_2D_2$ and is comprised between two horizontal hinge lines. Note that the fold length in Wierzbicki's model is half of the fold length in mine.

4.3.2 Analysis for thin foils

The basic assumptions made in Section 4.2 are retained for the analysis in this sub-section. It has been concluded by the careful examination of the crushing process that the creation of a hinge line implies an important out-of-plane deflection that is directly responsible for the next fold. The aim of this part is to model this and find out analytically where the next hinge lines appear by computing the plastic stresses induced in the model. Our set of boundary conditions will have to account for the studied effect. The schematic of the analysis is presented in Fig. 4.9. We choose to study only one plate at a time because it is not easy to adapt the following analysis directly to a *Y* configuration. The studied plate is the double thickness one, because we believe that this plate is the determining factor for the folding length. The limitation of the analysis to only one plate is clearly a limitation of the present analysis. We assume that the displacement of the plate is given as:

$$\omega = \omega_0 \cos(\frac{\pi x}{L}) f(y) \tag{4.3.1}$$

where $f(y)$ is an unknown function. Note that this assumption is very different from the previous one, which was deduced from using the boundary conditions in the elongated direction. In the present case, we do not know beforehand the shape of the plate in the elongated direction due to the boundary conditions (to be given in detail later). We assume that the shape of the plate is a cosine in the small direction, because it is primarily symmetric. However the hypothesis that we can separate the variables here is a very strong one, which is mainly responsible for the potential inaccuracy of the model.

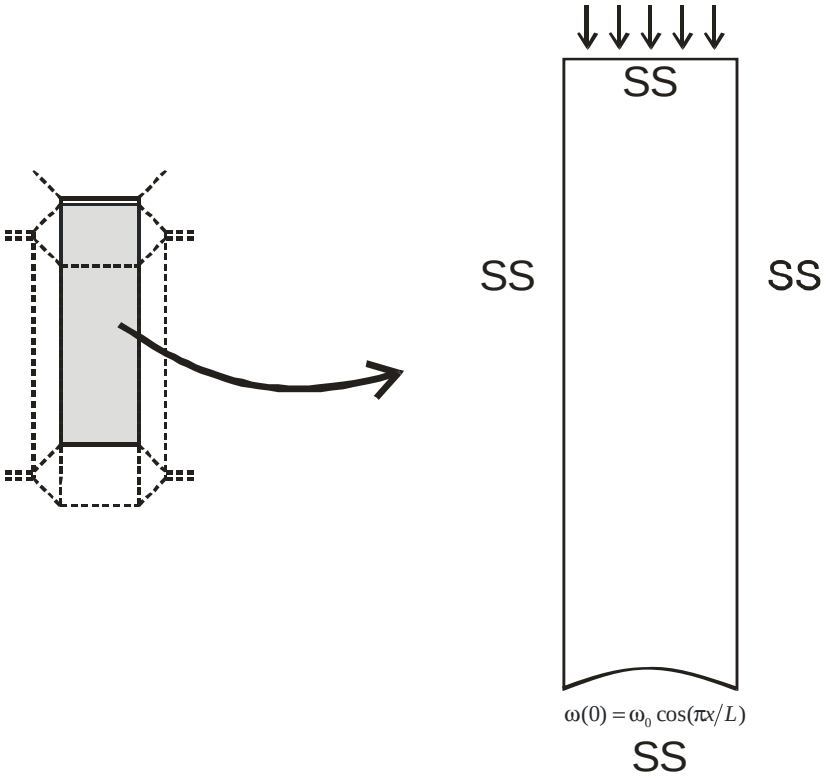

Fig. 4.9: Schematic of the delamination-based model for the analysis of the folding wavelength for samples with thin plates. Note that the plate shown has double thickness. The curve figured at the bottom of the plate figures an out-of-plane deflection (not a change in the shape of the plate, which remains rectangular).

From the equilibrium equation (Eq. 4.2.1) come the following equations:

$$f(y) = A_1 e^{r_1 y} + A_2 e^{r_2 y} + A_3 e^{r_3 y} + A_4 e^{r_4 y} \tag{4.3.2}$$

$$r_i^2 = -\left(\frac{\sigma t}{2D} - \frac{\pi^2}{L^2}\right) \pm \sqrt{\left(\frac{\sigma t}{2D} - \frac{\pi^2}{L^2}\right)^2 - \frac{\pi^4}{L^4}} \tag{4.3.3}$$

Introducing the classic parameter $K = \sigma t L^2 / \pi^2 D$, we obtain:

$$r_i^2 = \frac{\pi^2}{L^2}\left[\left(1 - \frac{K}{2}\right) \pm \sqrt{K\left(\frac{K}{4} - 1\right)}\right] \tag{4.3.4}$$

Depending on the value of *K*, the roots are either imaginary, have a real part or are real. We will give details of the different cases after introducing the boundary conditions. The four boundary conditions are as follows:

- for the edge $y = \Lambda$ (top edge), the boundary condition is not so important. We will use either fixed boundary condition or simply supported. This means that $\omega(y = \Lambda) = 0$ and either $\partial\omega/\partial y\,(y = \Lambda) = 0$ or $\partial^2\omega/\partial y^2\,(y = \Lambda) = 0$.
- for the edge $y = 0$, we assume a cosine deflection, i.e. $\omega(0) = \omega_0 \cos(\pi x/L)$ and complete with a simply supported type of boundary by stating that the moments on the boundary are zero. This gives $\left(\partial^2\omega/\partial y^2\right)(y = 0) + \nu\left(\partial^2\omega/\partial x^2\right)(y = 0) = 0$.

For the vertical boundaries the conditions are already implied by the form chosen for *w*. We can now start our analysis of the results by distinguishing the different cases implied by the value of *K*.

Case 1: $K > 4$

In this case the roots are imaginary, the function $f(y)$ can be written as

$$f(y) = A_1 \cos(\pi s_1\, y/L) + A_2 \sin(\pi s_1\, y/L) + A_3 \cos(\pi s_2\, y/L) + A_4 \sin(\pi s_1\, y/L) \qquad (4.3.5)$$

where $s_{1/2} = \sqrt{K/2 - 1 \pm \sqrt{K(K/4 - 1)}}$. The function is therefore non-attenuated, which does not fit with the experimental values of *K* and intuition. Therefore, this case is ignored in what follows.

Case 2: $K < 4$

In this case we have to rewrite r_i^2 as:

$$r_i^2 = \frac{\pi^2}{L^2}\left[\left(1 - \frac{K}{2}\right) \pm I\sqrt{K\left(1 - \frac{K}{4}\right)}\right] \qquad (4.3.6)$$

Note that we can write $r_i^2 = \pi^2/L^2 \cdot e^{I2\theta}$ and consequently $r_i = \pm\pi/L \cdot e^{\pm I\theta}$. Using trigonometric identities, it is easy to find all the quantities we need as $\cos(2\theta) = 1 - K/2$,

$\sin(2\theta) = \sqrt{K(1-K/4)}$, $\cos(\theta) = \sqrt{1-K/4}$ and $\sin(\theta) = \sqrt{K/4}$. The function $f(y)$ can now be rewritten as:

$$f(y) = e^{\pi\sqrt{1-K/4}\,y/L}\left(A_1\cos(\pi\sqrt{K/4}\,y/L) + A_2\sin(\pi\sqrt{K/4}\,y/L)\right) + e^{-\pi\sqrt{1-K/4}\,y/L}\left(A_3\cos(\pi\sqrt{K/4}\,y/L) + A_4\sin(\pi\sqrt{K/4}\,y/L)\right) \quad (4.3.7)$$

The boundary conditions can be written into a system given in Appendix 2. Note a major difference in the solution: here, we do not have a buckling problem as before, which required finding a bifurcation point. This meant finding a different solution than the trivial solution $X = 0$ to a problem of the type $AX = 0$ (A matrix, X vector of unknowns). Here, the problem can be written as $AX = B$ and we have to find the trivial solution $X = A^{-1}B$. It is easy to solve this system approximately in the case of plates with a large ratio $\phi = \Lambda/L$. Then the terms $e^{-\pi\sqrt{1-K/4}\phi}$ become negligible in front of the terms $e^{\pi\sqrt{1-K/4}\phi}$. Subsequently, we have $A_1 = A_2 = 0$, as well as $A_3 = 1$ and $A_4 = (1-\nu-K/2)/\sqrt{K(1-K/4)}$. Note that the solution is identical for the fixed end condition and the simply supported one for the edge $y = \Lambda$. Therefore, the unique solution is (slightly approximated, the real solution can easily be computed):

$$f(y) = e^{-\pi\sqrt{1-K/4}\,y/L}\left(\cos(\pi\sqrt{K/4}\,y/L) + \frac{1-\nu-K/2}{\sqrt{K(1-K/4)}}\sin(\pi\sqrt{K/4}\,y/L)\right) \quad (4.3.8)$$

This function has been plotted in Fig. 4.10 for the values $K = 1$ (red) and $K = 3$. We have now to describe what is exactly needed to create the next fold. Therefore, we have to study the state of stress in the plate. The plate stresses were given in 4.2.18, the plastic criterion in 4.2.19. Figure 4.11 presents a plot of the Von Mises stress for the previous two values of *K*. It can be seen that the figures are very different when *K* is smaller or larger than 2. If it is smaller, the stresses are nearly uniform on a line $y = Cst$, from which it is difficult to deduce anything. However, for all cases we have a local maximum of the stress at the negative peak (observed at the middle of the plate for *y*=0.7

for the case K=3). We believe that the next hinge line starts in this position while the creation of the folding mechanism is facilitated by the fact that the vertical boundaries of the plate become plastic very fast (the stresses are very large in these boundaries, and three plates are joined at the boundaries, which concentrates the stresses even more). The precise minimum of the Eq. (4.3.8) gives the value of $2H$. Therefore, the folding wavelength for thin foils λ_{mech} is

$$\lambda_{mech} = \frac{2L}{\pi\sqrt{K/4}}\left\{ ATAN\left(\frac{\alpha\sqrt{K/4} - \sqrt{1-K/4}}{\alpha\sqrt{1-K/4} + \sqrt{K/4}} \right) + \pi \right\} \tag{4.3.9}$$

where $\alpha = \frac{1-\nu-K/2}{\sqrt{K(1-K/4)}}$, $K = \frac{\sigma 2tL^2}{\pi^2 D}$, $D = \frac{E\cdot(2t)^3}{12\cdot(1-\nu^2)} = \frac{2Et^3}{3(1-\nu^2)}$.

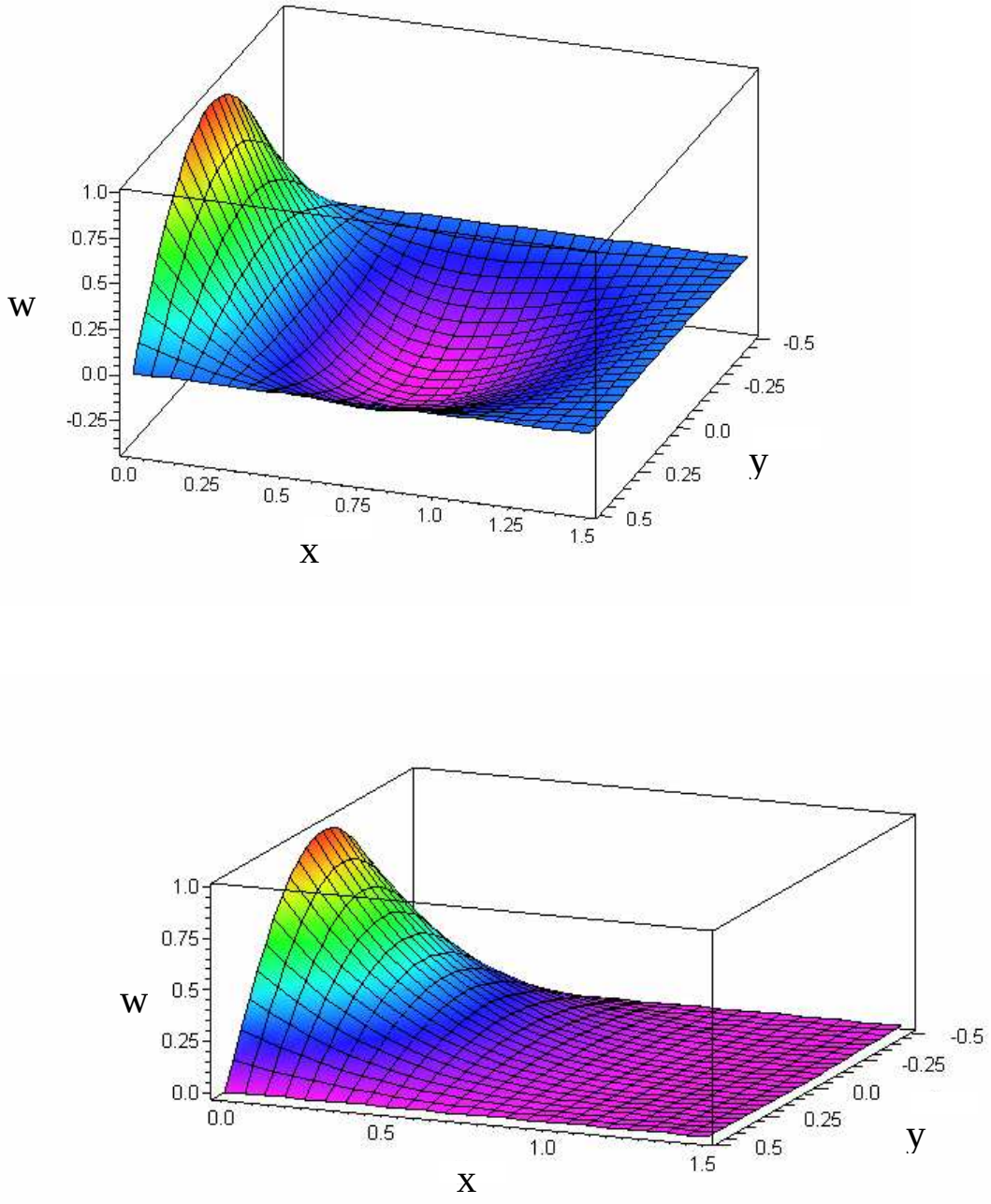

(b)

Figure 4.10: Displacement field for the cases K=3 (top) and K=1 (bottom). In both cases, there is a local minimum after the initial peak, it is just difficult to see on the second plot because it is so attenuated.

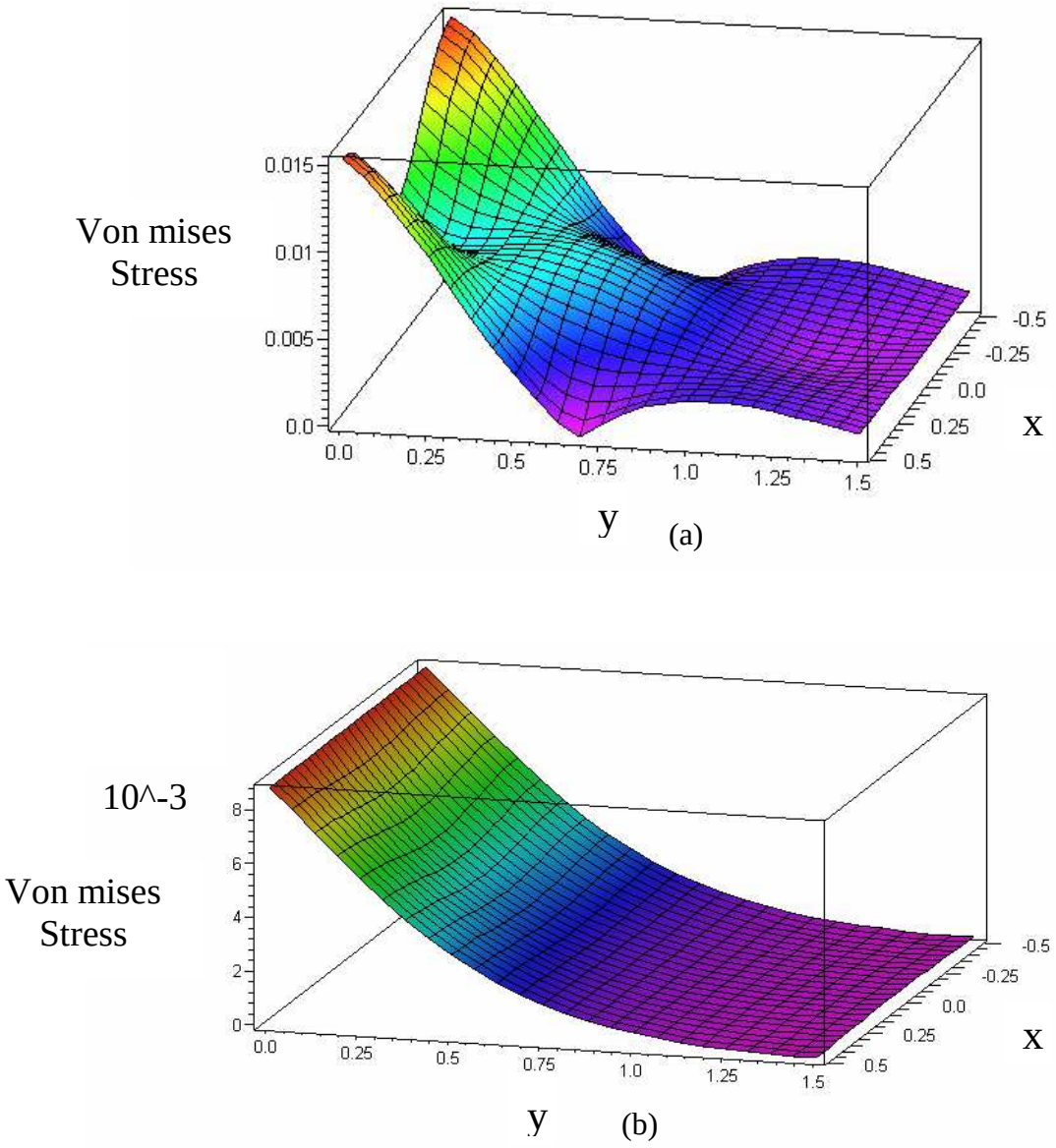

Fig. 4.11: Equivalent Von Mises stress for the cases *K*=3 (top) and *K*=1 (bottom). The case *K*=3 has a local maximum of the stress corresponding to the valley in Fig. 4.10a, at the center of the plate.

4.3.3 Thick foils

For samples with thicker walls it appears that the fold length is limited by the geometry of the problem. According to the previous theory, thicker walls imply larger folding wavelengths. However, a few drawings of the folding pattern show that the folding wavelength has a physical or geometric limit that we have to account for. Figure 4.12 presents different views of a sample when L is continuously decreased, which is in effect equivalent to increasing t. In this figure, the top view is presented as before in Fig. 4.3, while for the side view, we represent the hinge lines of a fold on an original non-folded configuration. It can be seen that there is a geometric limit to the folding wavelength.

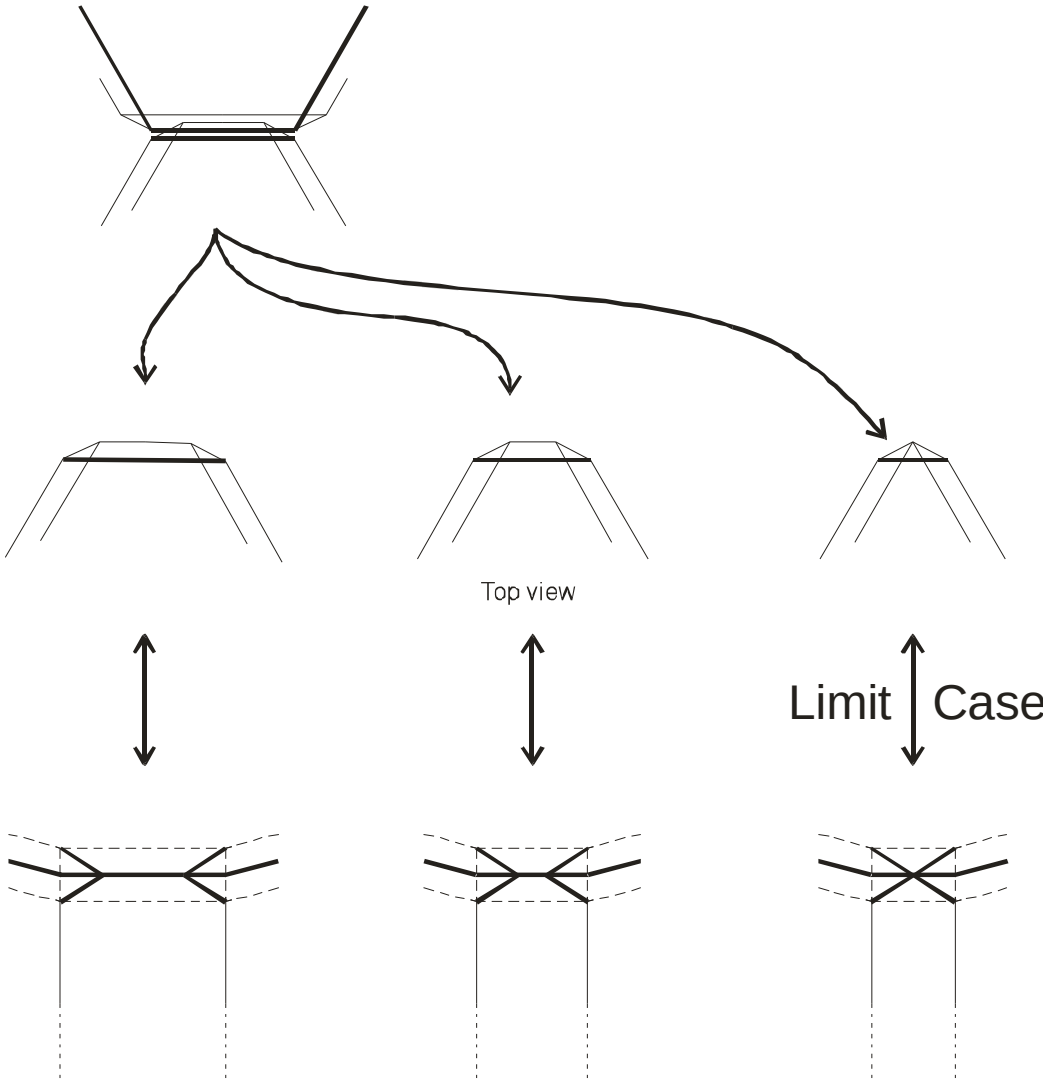

Fig. 4.12: Top views and side views of studied elements for decreasing cell sizes. The geometric limit is easy to identify on the right. The top view is identical to Fig. 4.3. The side view represents the folding pattern on an un-deformed configuration.

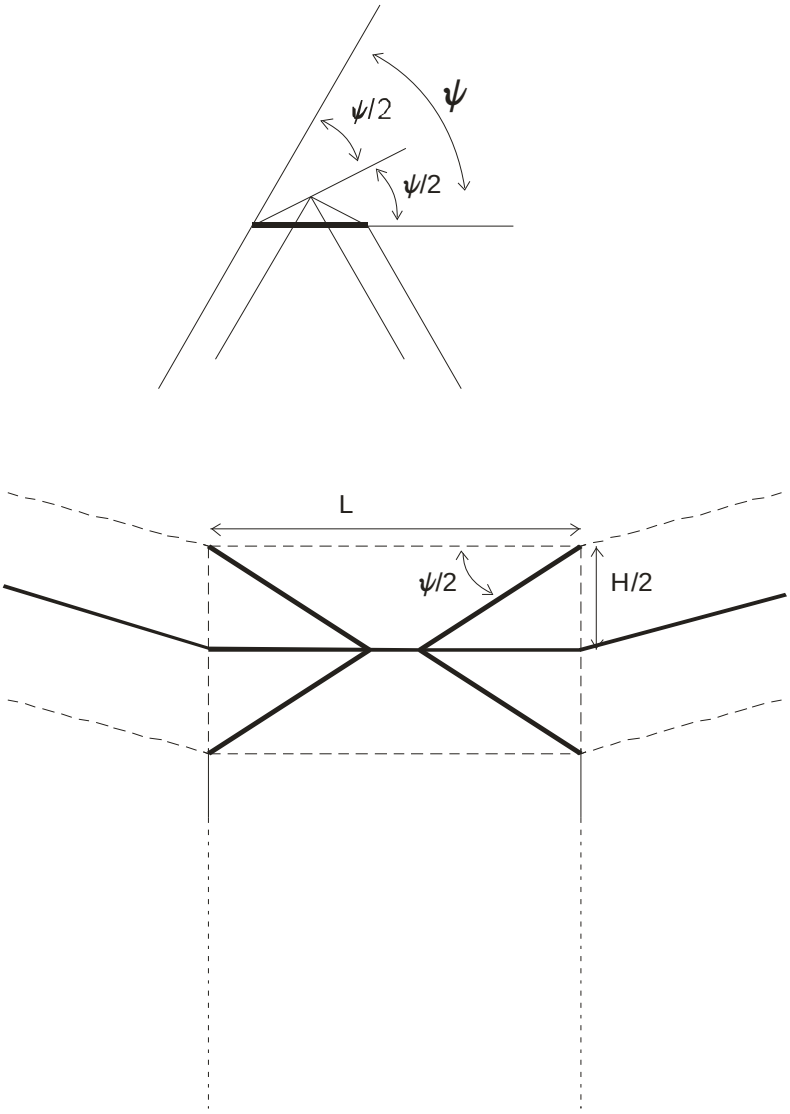

Fig. 4.13: Study of the geometric limit. The condition comes from writing the compatibility condition along the horizontal fold axis.

The computation of this limit is based on the sketches from Fig. 4.13. It is easy to see that the condition is:

$$H < \frac{L}{\sqrt{3}} \tag{4.3.10}$$

If we account for the thickness effects, stating that the fold can not reach the angle $\psi/2$ of Fig. 4.13 because of the thickness of the material, we are led to:

$$H < \frac{L}{\sqrt{3}} + t \tag{4.3.11}$$

To determine which of the two models has to be used for the computation of the folding wavelength, it is easy to find a criterion. We simply base our analysis on the fact that the first computation (for honeycomb made of thin plates) is based on a complete mechanics approach, whereas the second is a simple geometric limit. Therefore, as long as it is possible, the material will behave in the range of the mechanical model. As soon as it becomes geometrically impossible, the other model has to be used. That is to say, we use for *H* the minimum of the two solutions found before, Eqs (4.3.9) and (4.3.11). Thus, the folding wavelength for thicker foils λ_{geo} is given by

$$\lambda_{geo} = \frac{4L}{\sqrt{3}} + 4t \tag{4.3.12}$$

It must be noted that this second result corresponds only to a geometric limitation. However, we did not model this aspect of the problem here, which explains why our results do not fit with this limitation for thick foils.

4.4 Results and discussion

The comparison of the theories with experimental data is presented in Fig. 4.14. We also compare the data with Wierzbicki's (1984) folding height formula:

$$H = 0.821\sqrt[3]{tL^2} \tag{4.3.13}$$

Note that a folding wavelength in Wierzbicki's model $\lambda_{Wierzb.}$ is the height 2*H*:

$$\lambda_{Wierzb.} = 1.642\sqrt[3]{tL^2} \tag{4.3.14}$$

It can be seen that for samples with thin plates, our results are satisfactory, with a difference of 4.5 % for both 2.29 mm sample and 2.75 mm sample. Wierzbicki's model, as well as the buckling model, is not satisfactory. This shows first that the buckling pattern is not responsible for the fold length.

For thick samples, our computation, which is based here on the geometric limit, becomes inaccurate. Once again, it means that Eq. (4.3.12) is only a limitation but is not the result of the model of a physical behavior. The real understanding of the mechanics for thicker foils is a necessary future task. Our observations on thick samples show that some different buckling modes, which are of higher energy in the thinner foils and therefore not interesting, are generated for thick foils. From what we observed on the thick plates' samples, the folds are no longer horizontal but wavy. We believe that for ratios *t/L* lower than *2e-2*, these modes do not occur. Nevertheless, the model is plainly satisfactory, for a broad range of ratios *t/L*.

The previous results allow us to study a major parameter for the design of energy absorbers, which is the crushing distance (see Fig. 1.2). This parameter is in effect the difference between the original height of the sample and the height when densification occurs. From the previous results it is easy to derive the crushing distance l_0:

$$l_0 = \Lambda_0 - \frac{\Lambda_0 4t}{\lambda} \tag{4.3.15}$$

Indeed one fold corresponds to the thickness 4t, due to the superposition of the plates in the double thickness region. This result allows computing directly the energy dissipated by a given sample by multiplying the length l_0 by the crushing strength. Therefore it is a major parameter for the design of honeycomb energy absorbers.

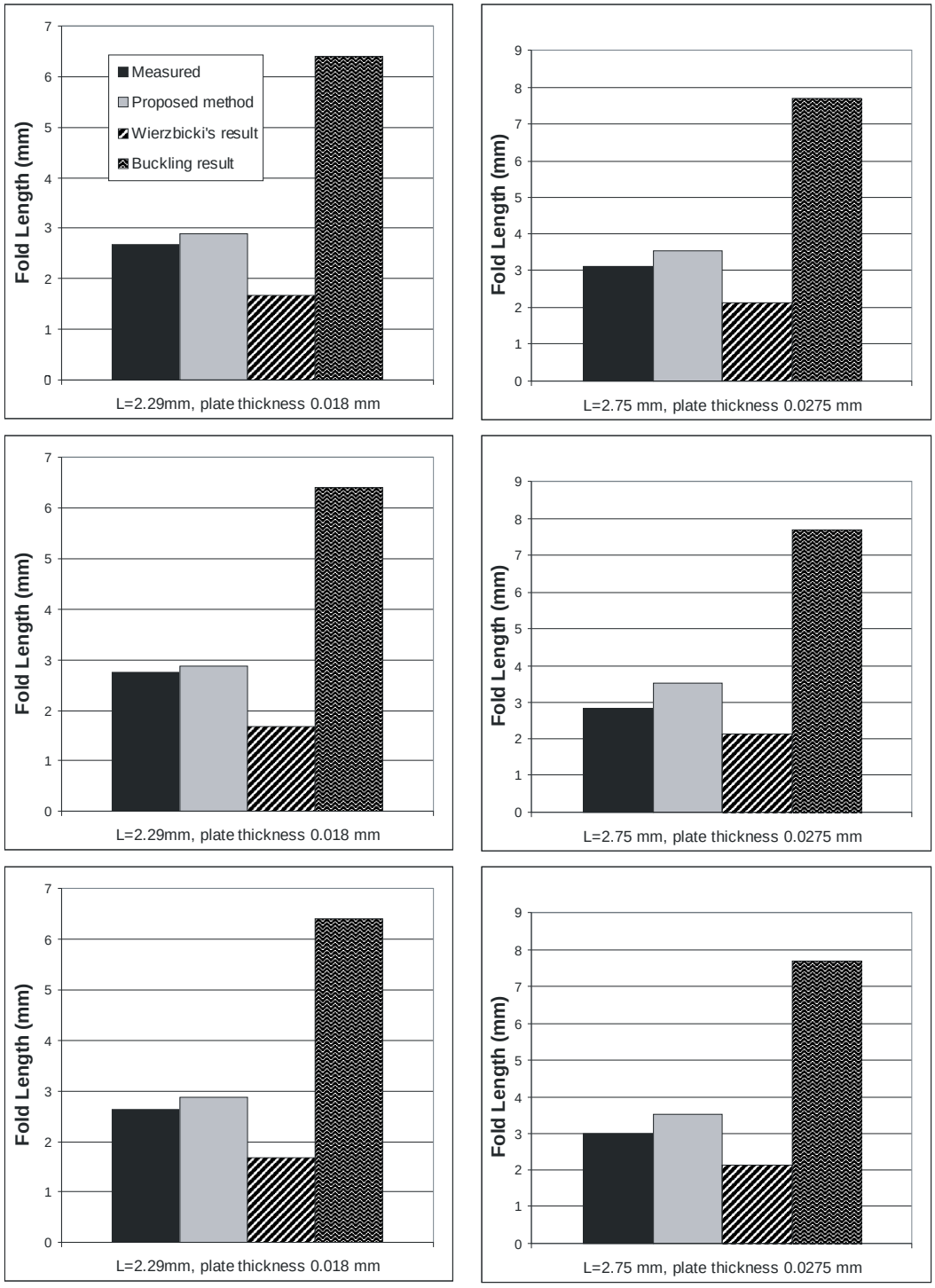

Fig. 4.14: Result of our study on the folding wavelength compared to our three set of experiments. The bars are in this order experimental result, result from the local model (part 4.3, Eq. 4.3.9), Wierzbicki's result (Eq. 4.3.14) and buckling result for the Y-element (Eq. 4.2.20).

4.5 Conclusions

The folding wavelength of ultra-light adhesive-joined honeycombs has been evaluated. It was found that partial delamination at highly stressed weaker sections of the honeycomb initiates the folding process and consequently leads to an accurate prediction of the folding wavelength. Although the correlation between buckling and folding patterns is rather intuitive, it is found that the hypothesis based on this assumption highly overestimates the folding wavelength. The present theory should be used keeping in mind its limitation for thicker plates when the fold front becomes highly irregular and the concept of fold length becomes highly local. However, for crushable ultra-light honeycombs, the result obtained in this paper is significant because it gives a better understanding of the folding kinematics, and allows the design of small layers of honeycomb, in which the crushing length is critical. Above all, it predicts the crushing distance, which helps to predict how much energy can be dissipated by the material. Therefore, the outcome of this work is significant for practical designs of lightweight components with crushable honeycomb cores.

5. Crushing regime

5.1 Introduction

The previous part has given us in depth understanding of what happens when the fold forms, especially in front of the folding front. Some side results have been derived, in particular the buckling strength and the crushing length. It is now time to study the bulk of the problem, which is the plateau stress. This part will use the results from section 4 as well as the understanding brought by Section 3. We use an energetic approach stating that the external energy is only due to the applied external crushing force and equating this energy to the energy dissipated in the plastic hinges for the folding of one fold. Thanks to periodicity the study is restrained to a *Y*-element and even further. Let's start now with the detail of the process. Keeping in mind our final objective, which is to evaluate the energy dissipated in the folding process for one fold, a classical mechanics approach would include the following:

1) Defining the precise geometry of the plastic region.
2) Defining the velocity field and the corresponding strain rates.
3) Using the plasticity flow rule to obtain stresses from velocities.
4) Computing the work at any time and deduce the total energy dissipated during the whole process.

However, we have here a set of problems which limits the precision of the work we can do by hand:

1) We don't know the exact geometry of the plastic region (microscopic phenomena) and therefore, have no option but to assume it. This means that in our model we assume the radii of curvatures; these radii are very small and would require measurements with an in-situ microscope to obtain an empirical law.
2) The velocity field is dependant on the geometry we use. We assume the geometry, and then assume a velocity field coherent with our geometry.
3) In plate theory, there is nothing like a plastic flow rule. Therefore, we will assume the direction of the stress and use the yield criterion to find its amplitude.

With the above considerations, we will be able to compute the energies. It can be noticed that this process is highly dependant on our intuition about the stresses, geometry,

and velocity field. This is probably the biggest limitation of our model, since most of the phenomena are microscopic and are not observed.

In addition, some other limitations arise from the following hypothesis:

(a) We work on a simplified thin plate model while neglecting the effects of the thickness.

(b) We study only the in-plane stresses. The out-of plane stress σ_{33}, as well as the "shear" stresses, σ_{13} and σ_{23} for the plate. are neglected. This is fine for very thin foils, which are the main focus of this paper.

(c) In the final balance of energy we neglect two sources of dissipation of energy, which are the energy necessary to break the bond between the plates and the heat produced by the folding process. We believe that these energies are negligible in comparison to the plastically dissipated energies.

(d) The material (typically aluminum or mild steel) is modeled as perfectly plastic. This is reasonable for aluminum but not for steel.

(e) We do not study 3D effects in the sense that in the real, non-modeled world, sections are only partially plastic. However, in our model, we always assume that a section is either not plastic at all ($\sigma < \sigma_0$ everywhere) or totally plastic ($\sigma = \sigma_0$ everywhere). This is reasonable as long as the size of the plastic zone is large compared to the thickness of the plates.

5.2 Geometry

We showed in Section 3 that our model evolves from Wierzbicki's by alternating the folds. However, it is also deeply asymmetric in the sense that the side of the horizontal hinge line which is on the already folded side is very different than the side on the intact part of the sample. For the analysis, it is however possible to neglect this aspect locally and use a symmetrical model similar to Wierzbicki's model, with a few adaptations to our new understanding. Considering that the *Y* element presented in Fig. 1.1 is made up of two plates bonded together, it is possible to build a model with only one plate. Indeed, the center of our study will be plastic dissipation in the plastic croissant (defined later), and for this aspect the two plates are exactly identical. However, for the study of the horizontal hinge lines, we will have to go back to the complete *Y* element.

Our model is presented in Fig. 5.1. The hinge lines in our model are shown as thick lines, while for the limits of the studied element we use dashed lines. Note that in our model the lines $A_1F_1D_1$ and $A_3F_3D_3$ are not plastic. The plastic regions are detailed in Fig. 5.2, where the arrows represent the local velocity field.

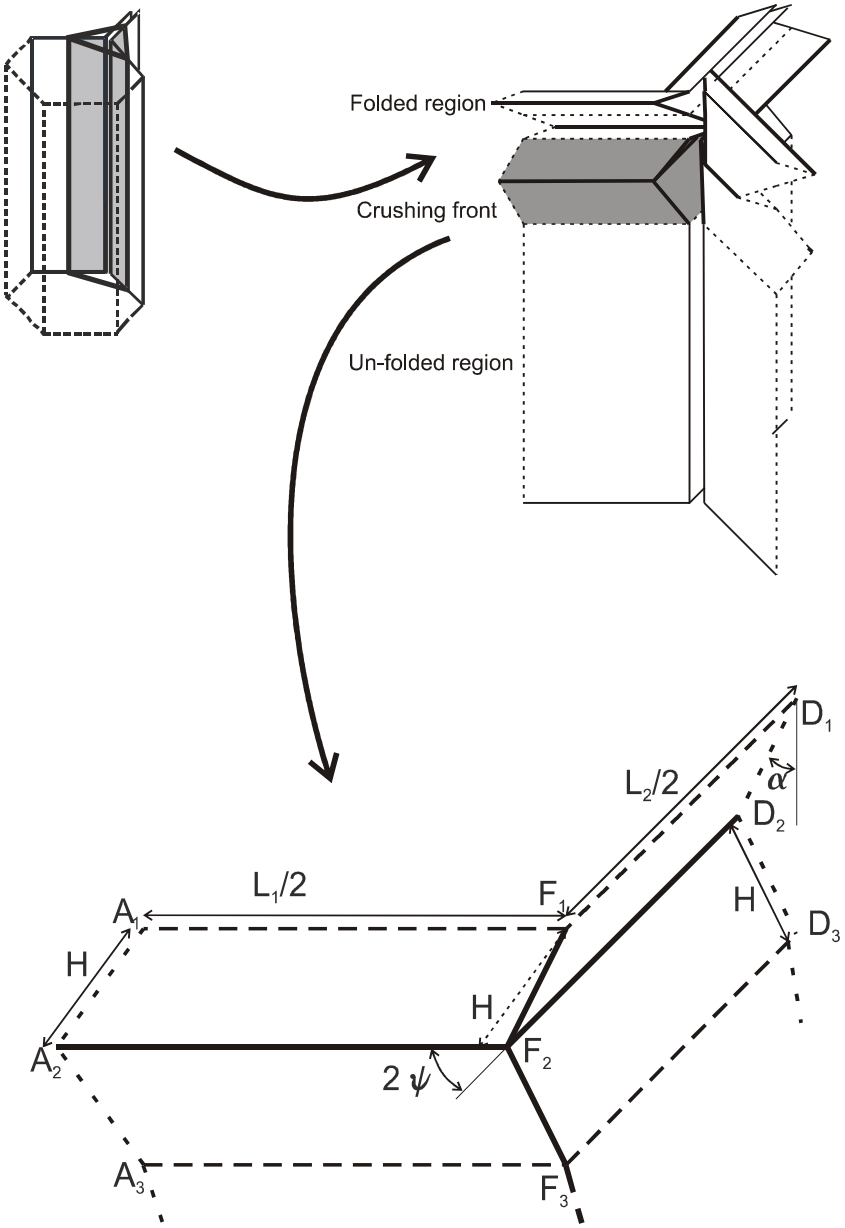

Figure 5.1: Notations used in this paper. We study only one plate from a *Y* element. The main angle used in the study is α, the angle between the vertical direction and the plate in a vertical cut.

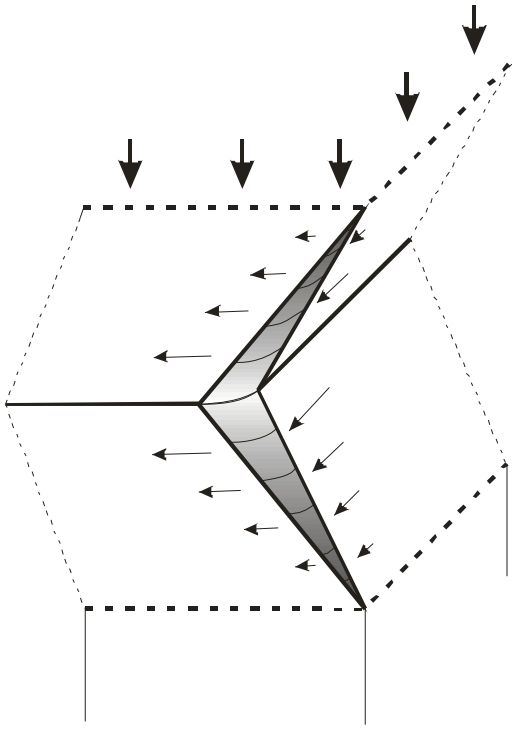

Figure 5.2: Detail of the plastic region. The arrows represent the local velocity field. The bold lines represent the plastic hinge lines, while the dashed lines are just the limits of the fold (not plastic)

The plastic regions comprise the following:

(a) one horizontal hinge line corresponding to $A_2F_2D_2$ in Fig. 5.1. The horizontal hinge line is responsible for the folding of the material. Note that there are no other horizontal hinge lines, although we have the same basic element as Wierzbicki.

(b) one large vertical plastic zone, which we think can be approached by a sort of croissant. This plastic croissant corresponds to the hinge line F_1FF_2 in Fig. 5.1.

A few comments are necessary here:

(a) As stated before, the studied figure admits a horizontal symmetry plane. Therefore, we will study only the top half of the depicted figure.

(b) The croissant part is made in our model of an ensemble of horizontal curves. The radii of curvature will vary in the horizontal plane as well as in the vertical direction. That is, unlike Wierzbicki's model, it is not axis-symmetric. Indeed the profile of the horizontal centers of curvature is not the line F_1F_2 (it is instead a

curve which ends in F_1 and F_2, one can be persuaded by looking at the sketch of the top view of the folding process).

In the following we will focus on the study of the croissant, which requires more work. Unless directly stated, we will always study the croissant.

Let us now determine mathematically the geometry of the plastic croissant. We choose to use cylindrical coordinates, the point M will be found by its horizontal radius of curvature r_H, horizontal angle θ, and vertical distance to the origin y (direction perpendicular to the horizontal direction and coplanar to it in the plane of the plate); the origin is taken at the horizontal symmetry plane, since we study only the top half of Fig. 5.1). The velocity field we assume allows us to consider that two points from the same initial horizontal section remain in the same horizontal plane. Therefore, we replace y by the parameter y_0 which is the same coordinate but at the beginning of the folding process, when $\alpha = 0$ (we have $y = y_0 \cdot \cos(\alpha)$).

The range of the variables for the top-half of the croissant is:

$$y_0 \in [0, H] \tag{5.2.1}$$

$$\theta \in [-\psi, \psi] \tag{5.2.2}$$

Let's first assume that the radius of curvature is constant in the horizontal plane. The radius of curvature is chosen as

$$r_H = r_0 \cdot (1 - \frac{y_0}{H}) \tag{5.2.3}$$

where r_0 is the horizontal curvature of the plate in F_2 (where this curvature is at its maximum).This formulation is approximated for the middle of the plate (where there is rotation around the horizontal axis).

5.3 Velocity field

We use here the original idea of Wierzbicki (see Fig. 5.3). We thus write the velocity field at a point M defined by y_0 and θ as:

$$\underline{v} = \frac{v_H}{\sin(\psi)}\underline{u}_X - \frac{v_H}{\tan(\psi)}\underline{u}_\theta - v_V\underline{u}_z \tag{5.3.1}$$

$$v_H = \cos(\alpha)\dot{\alpha}(H - y_0) \text{ and } v_V = \sin(\alpha)\dot{\alpha}(H + y_0) \tag{5.3.2}$$

v_H is the observed horizontal velocity, as shown in Fig. 5.3. This represents a pure rotation around point O' in the horizontal plane. Both the horizontal and vertical velocities are taken as linear functions of the vertical coordinate y_0.

This velocity field can be considered as being composed of a convective part $v_H\underline{u}_X/\sin(\psi) - v_V\underline{u}_z$ and a local velocity $v_H\underline{u}_\theta/\tan(\psi)$ responsible for the deformation of the plate. It can be seen that the velocity of the horizontal center of curvature is given by the convective part only, so that we consider only the other part for the computation of the strain rates. One can rewrite the local velocity as

$$\underline{v_{local}} = -v_t\underline{u_\theta} = -\frac{v_H}{\tan(\psi)}\underline{u_\theta} = -r_H\dot{\omega}\underline{u_\theta} \tag{5.3.3}$$

which corresponds to a simple rotation of rate $\dot{\omega}$, around the center of curvature O. Now we modify the previous hypothesis that the radius of curvature does not change in the horizontal plane. We use instead the following hypothesis:

$$r_H(\theta) = (\bar{r} + \Delta r\frac{\theta}{2\psi})(1 - \frac{y_0}{H}) \tag{5.3.4}$$

$\bar{r} = (r_{\min} + r_{\max})/2$ is the average of $r_H(\theta)$ and $\Delta r = r_{\max} - r_{\min}$ is the variation of $r_H(\theta)$

The two parameters $r_{\max}$ and $r_{\min}$ will be determined later. The radius of curvature depends linearly on θ and is taken to be bigger on the edge of the croissant

which is moving forward. This accounts for the moments that are much higher close to this edge and therefore induce much larger rotation. We make the assumption that the velocity field computed before is not much changed by the modification of the horizontal geometry (except that the vector $\underline{u_\theta}$ is changed).

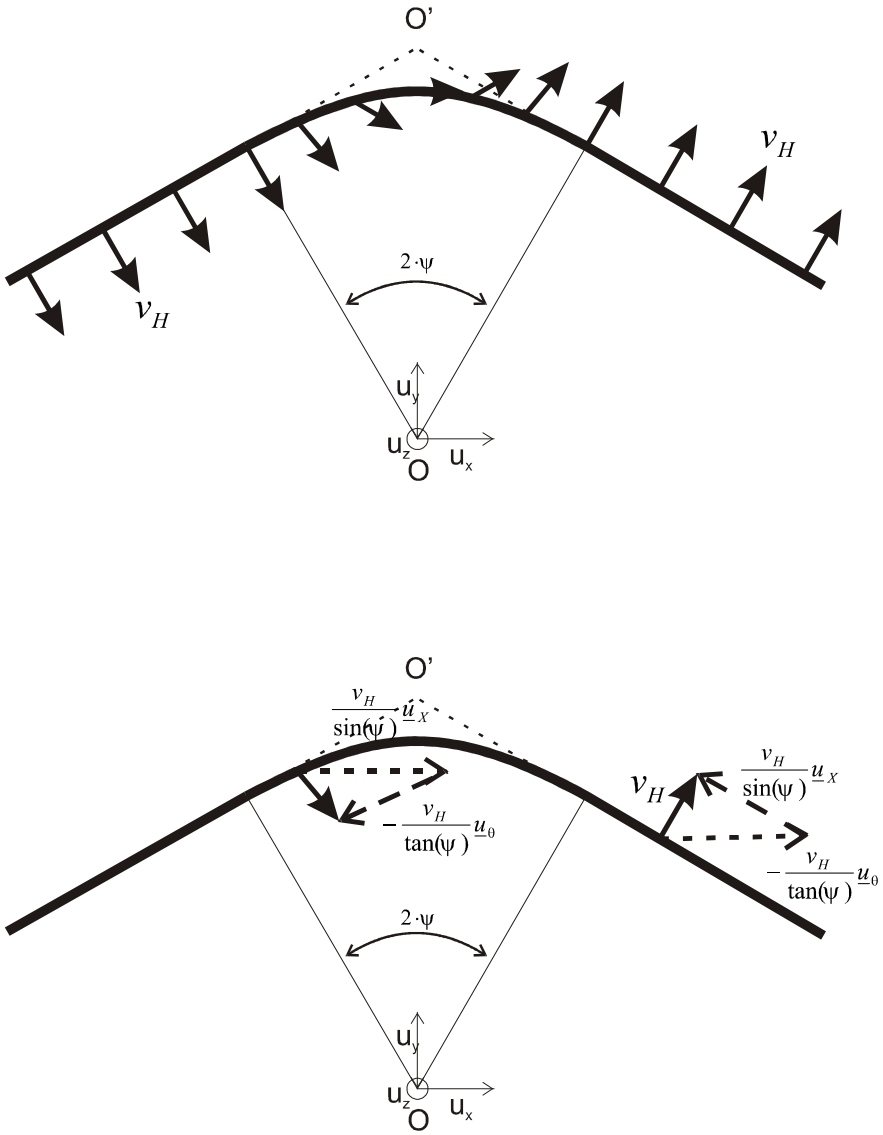

Figure 5.3: Horizontal speeds. The speeds are composed of a convective speed and a local speed responsible of the deformation.

We can compute now the strain rates and the rates of change of curvatures for the croissant (the horizontal hinge lines will be studied separately). The only needed strain rates will be, as shown in the next part, the horizontal strain rate $\dot{\varepsilon}_{11}$ and rate of change of curvature $\dot{\kappa}_{11}$ (one corresponds to the local horizontal tangent direction of the plate). One finds:

$$\dot{\varepsilon}_{11} = \frac{v_t}{r_H^2}\frac{\partial r_H}{\partial \theta} \tag{5.3.5}$$

$$\dot{\kappa}_{11} = \frac{v_t}{r_H}\frac{\partial(1/r_H)}{\partial \theta} \tag{5.3.6}$$

5.4 Plastic flow

Note that these fields are local, i.e. they depend on both θ and y_0. We can now express the plastic flow rule condition for plates and apply it to our problem. *N* corresponds to the plate resultants while *M* corresponds to the plate moments (both are integrals of the local stress field $\underline{\underline{\sigma}}$ throughout the thickness of the plate).

For a thin, totally plastic plate, the yield criterion is

$$f(N,M) = \frac{N^2}{N_0^{\,2}} + \left|\frac{M}{M_0}\right| - 1 = 0 \tag{5.4.1}$$

We would have to use the flow rule to find the direction of the force in *3D*. However, we can't use that in a plate theory (no general flow rule). We replace this by a set of assumptions. For the croissant, we make the assumption that the stress is mainly in the horizontal tangent direction, since the deformation of the croissant is mainly horizontal. The only part where this assumption is a problem corresponds to the middle of the croissant, where there is an important change in the vertical curvature. We neglect this aspect. Additionally, we neglect in the croissant N_{22}, N_{12}, as well as M_{22} and M_{12} (where 2 corresponds to the tangent pseudo-vertical direction for the plate, while 1

corresponds to the horizontal direction for the plate); we still have two general stresses N_{11} and M_{11} related by Eq. 5.4.1. We justify this by assuming that the forces that stretch the croissant in the horizontal direction are the ones that effectively make it move and therefore are the largest.

We now compute the state of stress in any point of the croissant. Using the hypothesis of fully plastic sections, the moment M_{11} and axial force N_{11} can be expressed as functions of the radius of curvature. See Fig. 5.4 for a model of the forces in a section, where the forces have been drawn directly at the place of a section.

$$N_{11} = \begin{cases} 2 \cdot \sigma_0 \cdot r_H = N_0 \cdot \dfrac{2 \cdot r_H}{t} & \text{if} \quad r_H \le t/2 \\ \sigma_0 \cdot t = N_0 & \text{if} \quad r_H > t/2 \end{cases} \tag{5.4.2}$$

$$M_{11} = \begin{cases} \sigma_0 \cdot \dfrac{t^2}{4} \cdot (1 - \dfrac{4 \cdot r_H{}^2}{t^2}) = M_0 \cdot (1 - \dfrac{4 \cdot r_H^2}{t^2}) & \text{if} \quad r_H \le t/2 \\ 0 & \text{if} \quad r_H > t/2 \end{cases} \tag{5.4.3}$$

Therefore, the moment is much more important when the radius of curvature is small, while the axial force is dominant when the radius of curvature grows.

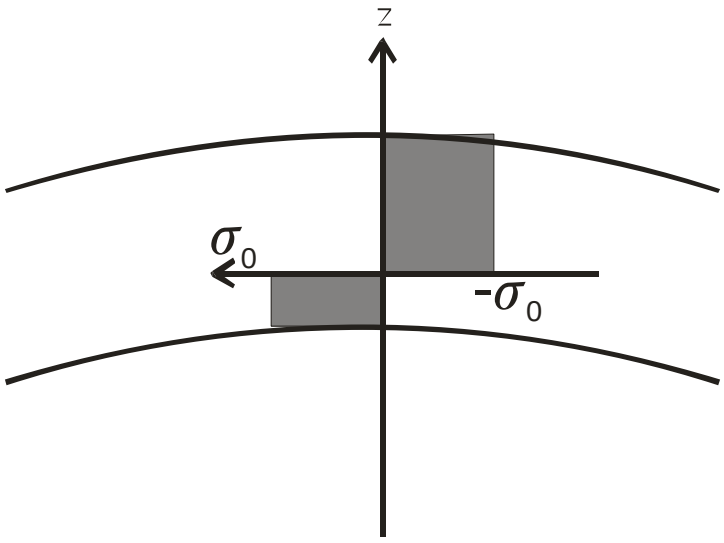

Figure 5.4: Representation of the stresses for a typical section in the direction of the thickness. The curved lines represent the limits of the plate.

Let us compute now the strain and stress fields for the horizontal hinge line $A_2F_2D_2$. This problem is a typical hinge line problem, and we use the common hypothesis of perfectly plastic sections. Therefore, the deformation is localized in an originally very thin stripe, which undergoes large deformations as the hinge line rotation grows larger. The hinge line is presented in Fig. 5.5 for an advanced deformation of the hinge line. Locally, the deformation is only due to stretching, the radius of curvature is constant. Hence, we need to compute the strain rate for the horizontal hinge lines. One gets:

$$\dot{\varepsilon}_{11} = \cos(\alpha) \cdot \dot{\alpha} \tag{5.4.4}$$

The plastic stress is thought to be only a tensile force equal to σ_0.

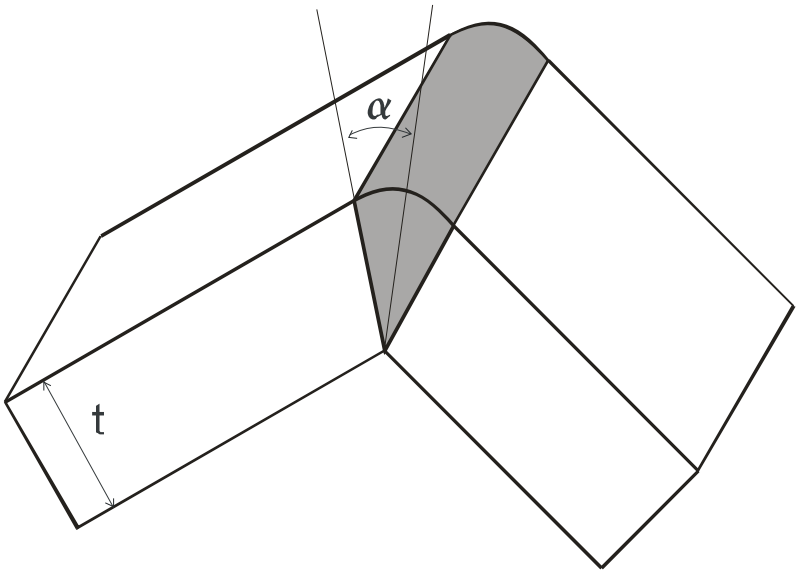

Figure 5.5: Representation of the plastic region for the horizontal hinge lines. The grey region figures the plastic region. The deformation is localized originally in a very thin layer, which undergoes very large deformations.

Before we go into the final computation of the dissipated energies, we have to determine our radii of curvature $r_{\min}$ and $r_{\max}$ for the plastic croissant. In the best case we would study that using a microscope. However, it is very difficult to do and we finally

chose to take values that appear coherent with the rest of the study. Hence, we will welcome any further study of this parameter. We chose in this study radii of curvatures $r_{\min} = t/2$ and $r_{mzx} = 1.5t/2$. This corresponds to a region where the axial forces are dominant.

5.5 Plastic dissipation in the plastic croissant

We compute in this part the work at any time by integrating the local work and deduce the energy by integrating in time. As mentioned before, we split the plastic zone into two parts, Zone 1 which is the croissant, and Zone 2 which is the horizontal hinge line. Because of symmetry, we compute the energy dissipated in the top half of the structure, which corresponds to the height H using the notations of Fig. 5.1.

The energy dissipated in the croissant is given as:

$$W_1 = \int (N \cdot \dot{\varepsilon}_{11} + M \cdot \dot{\kappa}_{11}) dS \tag{5.5.1}$$

where the surface element is given as $dS = r_H \cos(\alpha) d\theta dy_0$

Using Eq. (5.2.1), (5.2.2), (5.3.4), (5.3.5), (5.3.6), (5.4.2) and (5.4.3), and performing the integration one gets

$$W_1 = \frac{4H^2 \Delta r}{\tan(\psi)} \left[\frac{1}{\bar{r}^2 - \Delta r^2} + \frac{1}{3} \frac{1}{t^2} \right] M_0 \cos^2(\alpha) \dot{\alpha} + \frac{2}{3} \frac{H^2 \Delta r}{t \tan(\psi)} N_0 \cos^2(\alpha) \dot{\alpha} \tag{5.5.2}$$

$$E_1 = \frac{\pi H^2 \Delta r}{\tan(\psi)} \left[\frac{1}{\bar{r}^2 - \Delta r^2} + \frac{1}{3} \frac{1}{t^2} \right] M_0 + \frac{\pi}{6} \frac{H^2 \Delta r}{t \tan(\psi)} N_0 \tag{5.5.3}$$

This energy is the energy dissipated for the half of the plastic croissant illustrated in Fig. 5.2.

5.6 Fold length

The folding length *H* is given in Section 4 of this report as the minimum of the two following functions (5.6.1) and (5.6.2):

$$H = \frac{L_1}{\sqrt{3}} + t \tag{5.6.1}$$

$$H = \frac{L_1}{2\pi\sqrt{K/4}} \left\{ ATAN\left(\frac{\alpha\sqrt{K/4} - \sqrt{1-K/4}}{\alpha\sqrt{1-K/4} + \sqrt{K/4}} \right) + \pi \right\} \tag{5.6.2}$$

Where $\alpha = \frac{1-\nu-K/2}{\sqrt{K(1-K/4)}}$, $K = \frac{\sigma 2tL_1^{\,2}}{\pi^2 D}$, $D = \frac{E\cdot(2t)^3}{12\cdot(1-\nu^2)} = \frac{2Et^3}{3(1-\nu^2)}$ (5.6.3)

The function (5.6.2) corresponds to small ratios thickness t on cell size L_1, it comes from a mechanical analysis of the deformations of the sample under particular boundary conditions. On the contrary, Eq. (5.6.1) is due to only to geometric limitations in the folding process. Indeed a precise analysis has been conducted for the small thicknesses but not for the large ones, therefore Eq. (5.6.2) is a precise result while Eq. (5.6.1) is only an upper boundary for H.

5.7 Plastic dissipation in the horizontal hinge lines

For the dissipation due to the horizontal hinge lines, we refer to Fig. 5.6. The hinge line is idealized using the perfectly plastic assumption as a very thin layer of plastic material which undergoes large deformations. Let us suppose that the length of the hinge line does not change. Then, for a given angle of rotation of the hinge line α the dissipation can be written as:

$$E = \int \sigma_0 dldS = \sigma_0 L_{line} S_{plastic} = \sigma_0 L_{line} t^2 \alpha \tag{5.7.1}$$

The corresponding work is therefore $W = \sigma_0 L_{line} t^2 \dot{\alpha}$, and if we include some potential changes in the length of the hinge line, then we obtain:

$$W = \sigma_0 L_{line} t^2 \dot{\alpha} + \sigma_0 \frac{\partial L_{line}}{\partial \alpha} t^2 \dot{\alpha} \tag{5.7.2}$$

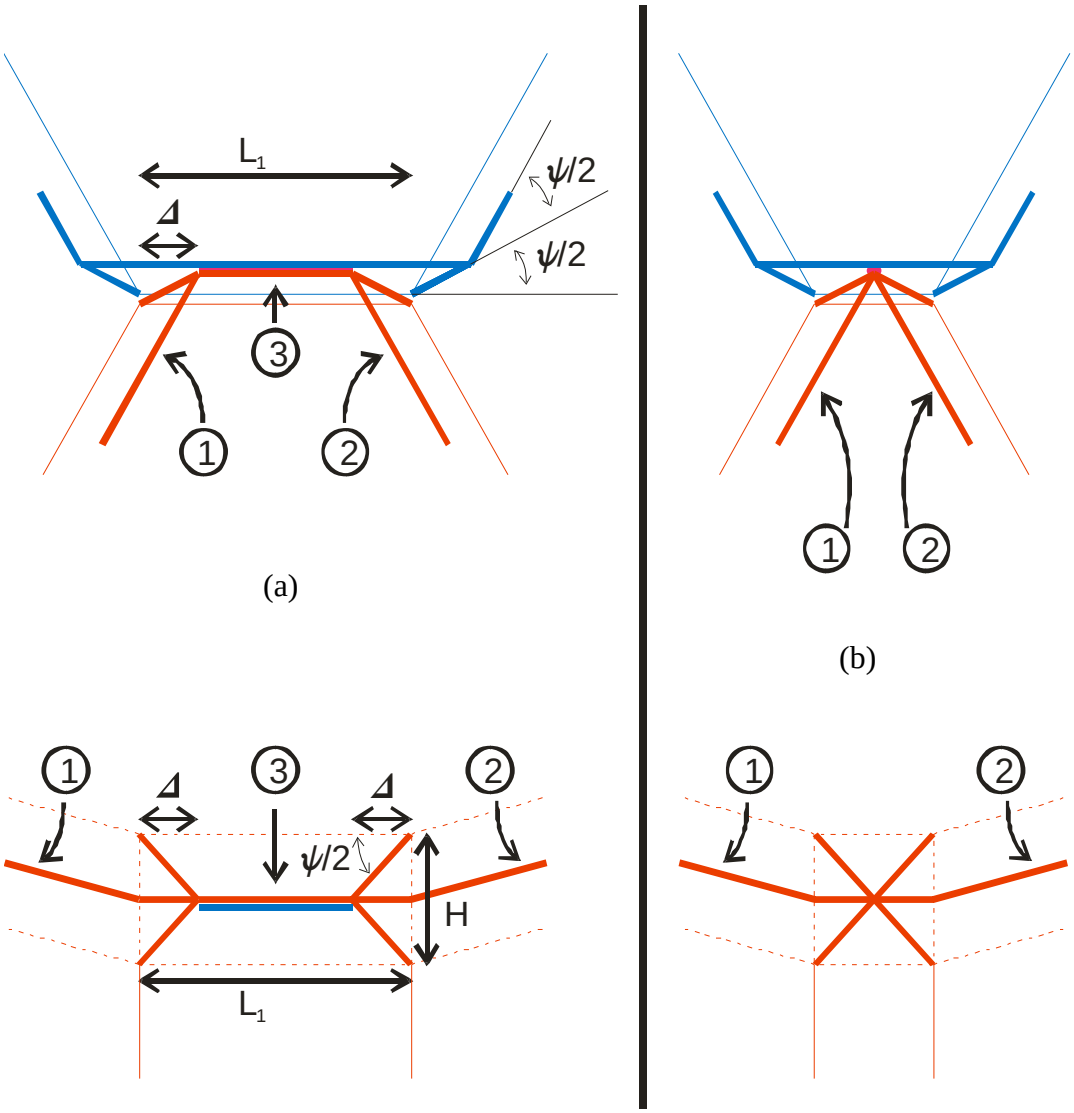

Figure 5.6: Hinge line for the two cases of Eq. (5.6.2) (mechanic limit: (a)) and (5.6.1) (geometric limit: (b)). This schematics is the final state when the fold is completely folded. The top two schematics are top views (in the tubular direction) while the two bottom views are side views (perpendicular to the tubular direction).

We need now to describe precisely what the geometry of the different hinge lines is. Two cases have to be considered because of the two potential cases of the computation of the hinge line (equations (5.6.1) and (5.6.2)). These two cases are the usual case and the case where a geometric limit appears (they are both illustrated in Fig. 5.6, which presents the top and side views of the studied element for the two cases). The side view is projected on the un-deformed configuration. We use the notations introduced previously.

In all cases, we can count two horizontal hinge lines in plates of thickness *t* numbered 1 and 2 in Fig. 5.6. Depending on the case, there is or not at the end of the folding an additional hinge line 3 in the plate of thickness *2t*. It can be seen that the sum of the lengths of the hinge lines 1 and 2 at the end of the folding process is $L_2 + 2\Delta$ where $\Delta = \sqrt{3}(H-t)/2$. In the case where there is a double thickness hinge line, its final length is $\left(L_1 - \sqrt{3}(H-t)\right)/2$. We make the assumption that during the folding process the lengths are linear functions of the folding angle, i.e. the length of the sum of hinge lines 1 and 2 is $L_2 + 2\Delta 2\alpha/\pi$ and the length of hinge line 3 is $L_1/2 - \sqrt{3}(H-t)\alpha/\pi$ in the normal case and $L_1(1-2\alpha/\pi)/2$ in the case where the geometric limit appears.

Using (5.7.2), the dissipated energy in the horizontal hinge lines is computed as:

$$E_2 = N_0 t\left(\frac{\pi}{2}L_2 + L_1\pi - \sqrt{3}\frac{\pi}{4}(H-t)\right) \qquad \text{for the mechanical limit} \qquad (5.7.3a)$$

$$E_2 = N_0 t\left(\frac{\pi}{2}(L_2 + L_1) + \sqrt{3}\frac{\pi}{4}(H-t)\right) \qquad \text{for the geometric limit} \qquad (5.7.3b)$$

5.8 Crushing force

The dissipated energies for the *Y* element are the energy dissipated in the croissant (remember we only computed the energy dissipated in one half of one plastic croissant, although the *Y* element comprises two complete croissants) and the energy dissipated in the horizontal hinge lines. That is:

$$E_{tot} = 4E_1 + E_2 \qquad (5.8.1)$$

The crushing force is derived by considering that the total energy dissipated for one fold comes from the external work from the vertical applied force.

$$E_{tot} = W_{ext} = \sigma S_{nom} 2H \qquad (5.8.2)$$

$$S_{nom} = 2\left(\frac{L_1}{2} + \frac{L_2}{2}\sin(\psi)\right)L_2\cos(\psi) \qquad (5.8.3)$$

S_{nom} is the horizontal tributary surface corresponding to the *Y* element. It can be seen that this surface is double of the area covered by the *Y* only, due to the holes of the structure. This gives the flowing final relation:

$$\sigma = E_{tot} \frac{1}{4HS_{nom}} \tag{5.8.4}$$

5.9 Results and discussion

All the results are given here using the hypothesis $L_1 = L_2 = L$ and $\psi = \pi/3$. The results are compared with the results given by Hexcel Corp in the HexWeb® Honeycomb Attributes and Properties. The values from Hexcel are simply converted to the standard international unit system. The result of the comparison is given in Fig. 5.7. Note that the analytic values obtained with Eq. (5.6.2) are presented with a bolder line while the results using Eq. (5.6.1) are given using a dotted line.

The results are very interesting for samples which use Eq. (5.6.2), but are not so close for samples using Eq. (5.6.1). For most values the error is less than 10% for the results using Eq. (5.6.2) as compared to Hexcel tests, and for all less than 25%. For results using Eq. (5.6.1) some large errors appear, as seen in Fig. 5.7.

We believe that our results are very satisfactory for honeycomb made of thin foils, which are also the most useful ones for applications needing light-weight materials. For thicker plates, the result for the fold length given by Eq. (5.6.1) is only an upper boundary, which was not relevant with the measures we made for thick samples. *We believe that thicker samples require a different analysis, since the folding mode is different.* An observation of a folded sample in this case shows that the folds tend to be slanted and not horizontal. This is allowed by the large thicknesses that allow the creation of some different folding patterns. Therefore, a new analysis would be required to fully understand the fold length in the case of the thick plates. It could be beneficial then to study if this theory still gives good results or not for the modified fold length (in the thick plates' case).

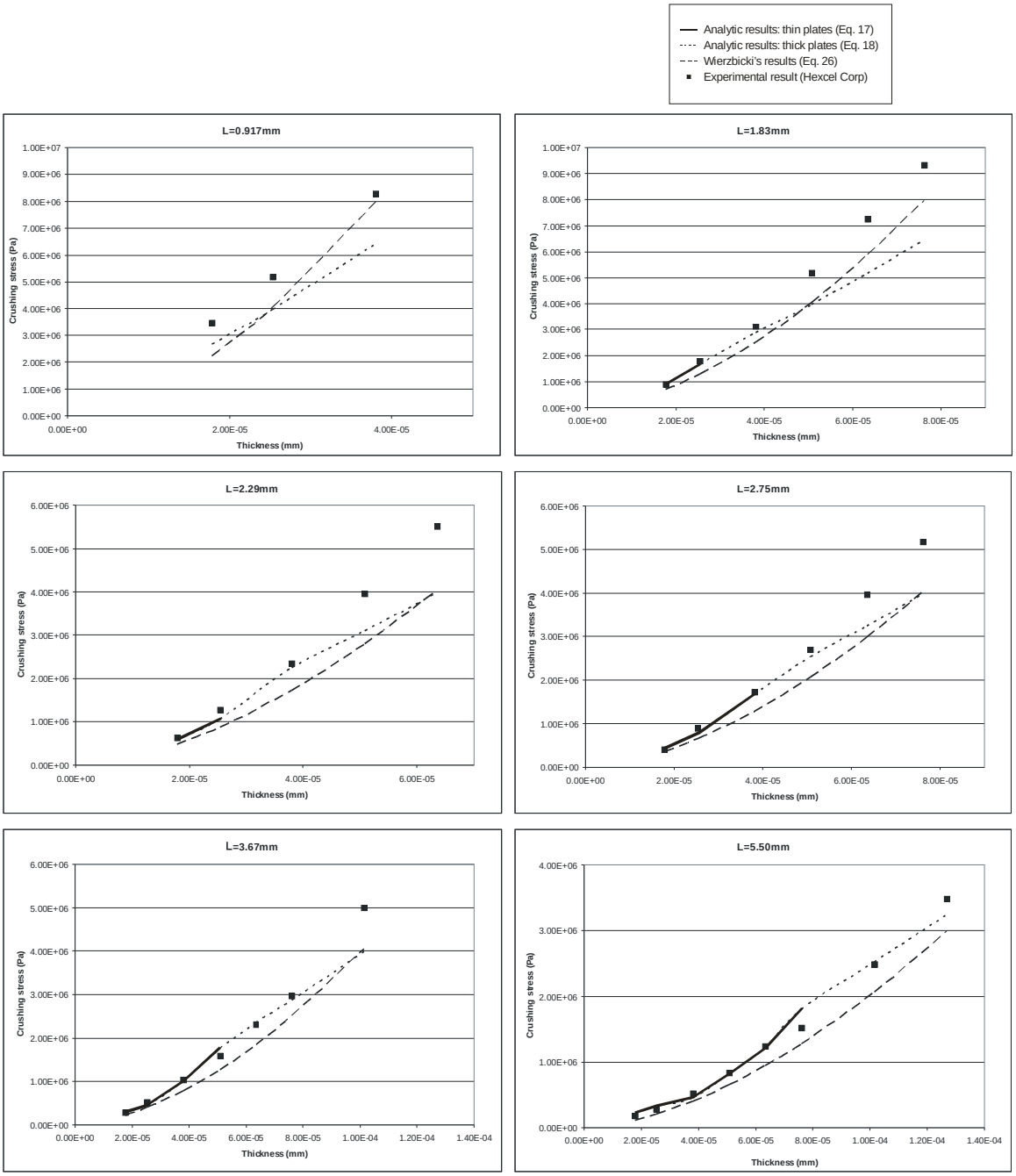

Figure 5.7: Comparison of the crushing stresses. The bold lines correspond to the case where we use Eq. (5.6.2) (thin plates) while the dotted ones correspond to the case where we use Eq. (5.6.1). The bold line gets longer as L gets larger, since the limit between the two cases depends only, when the material is fixed, of the ratio t/L.

The equation obtained by Wierzbicki for the crushing strength is as follows:

$$\sigma = \frac{1}{S_{nom}} 8.61 \sigma_0 \left(t^5 L\right)^{1/3} \tag{5.9.1}$$

It can be seen that it constantly underestimates the crushing stress by factors comprised between 15% and 40%. The present model for thin plates is a lot more precise than Wierzbicki's model and should be used alone. For thick plates, for most cases it is closer to the data than Wierzbicki's result.

Steps needed to compute the sustained crushing strength according to the present model are as follows:

1) Determine which case (Eqs. (5.6.1) or (5.6.2)) has to be used. Use an estimate (interpolation between known values) or an experimental result for σ, deduce K through Eq. (5.6.3). Compute H through Eq. (5.6.1) and (5.6.2) and determine which case is the right one. It is also possible to assume which case it is using the results of this study and by computing the ratio t/L of the samples. In this study we found that samples with ratio larger than 1.50e-2 are found to show the geometric limit. However this is only valid for this alloy, but can be used as a first approximate.
2) Compute E_1 through (5.5.3), E_2 through either (5.7.3) and deduce E_{tot}.
3) Compute S_{nom} through (5.8.3) and end up with σ using (5.8.4).

5.10 Conclusions

We present in this part of the thesis a model to compute the sustained crushing strength of adhesively-bonded metallic honeycombs that are used for shock and energy absorption. The derivation uses an energetic balance between the external and internally dissipated works. This requires definitions of proper geometry, kinematics, and stress field. The results are found to be very satisfactory for honeycombs with thin walls, which are also the most common in light-weight applications. For honeycombs made with thicker foils, the result is found to be less precise but to improve the past results. A more

precise study of these honeycombs would probably be necessary. However, it would face one of the main limitations of this paper, which is the hypothesis of totally plastic sections. The second limitation is the difficulty of studying one of the parameters of the problem, which is the radius of curvature of the plate in the plastic region. This parameter is a crucial one, and had to be assumed in this study.

Appendix

1) System solved in Section 4.2 for the *Y*-element

$$\begin{bmatrix} \cosh(\alpha_1) & \cos(\beta_1) & 0 & 0 & 0 & 0 \\ 0 & 0 & \cosh(\alpha_2) & \cos(\beta_2) & 0 & 0 \\ 0 & 0 & 0 & 0 & \cosh(\alpha_2) & \cos(\beta_2) \\ -\alpha_1\cdot\sinh(\alpha_1) & \beta_1\cdot\sin(\beta_1) & \alpha_2\cdot\sinh(\alpha_2) & -\beta_2\cdot\sin(\beta_2) & 0 & 0 \\ -\alpha_1\cdot\sinh(\alpha_1) & \beta_1\cdot\sin(\beta_1) & 0 & 0 & \alpha_2\cdot\sinh(\alpha_2) & -\beta_2\cdot\sin(\beta_2) \\ D_1(\alpha_1)^2\cosh(\alpha_1) & D_1(\beta_1)^2\cos(\beta_1) & D_2(\alpha_2)^2\cosh(\alpha_2) & D_2(\beta_2)^2\cos(\beta_2) & D_2(\alpha_2)^2\cosh(\alpha_2) & D_2(\beta_2)^2\cos(\beta_2) \end{bmatrix} \begin{pmatrix} A_{11} \\ A_{12} \\ A_{21} \\ A_{22} \\ A_{31} \\ A_{32} \end{pmatrix} = 0$$

Where $\alpha_1 = \frac{m\pi}{2\phi}\sqrt{1+\sqrt{K}\,\frac{\phi}{m}}$, $\alpha_2 = \frac{m\pi}{2\phi}\sqrt{1+\sqrt{K}\,\frac{\phi}{2m}}$, $\beta_1 = \frac{m\pi}{2\phi}\sqrt{\sqrt{K}\,\frac{\phi}{m}-1}$, $\beta_1 = \frac{m\pi}{2\phi}\sqrt{\sqrt{K}\,\frac{\phi}{2m}-1}$, $D_1 = \frac{E(2t)^3}{12(1-\nu^2)}$, $D_2 = \frac{Et^3}{12(1-\nu^2)}$

2) System solved in Section 4.3

$$\begin{bmatrix} 1 & 0 & 1 & 0 \\ 1-\frac{K}{2} & \sqrt{K\left(1-\frac{K}{4}\right)} & 1-\frac{K}{2} & \sqrt{K\left(1-\frac{K}{4}\right)} \\ e^{\alpha}\cos(\beta) & e^{\alpha}\sin(\beta) & e^{-\alpha}\cos(\beta) & e^{-\alpha}\sin(\beta) \\ e^{\alpha}\left[\cos(\beta)\left(1-\frac{K}{2}\right)-\sin(\beta)\cdot\sqrt{K\left(1-\frac{K}{4}\right)}\right] & e^{\alpha}\left[\sin(\beta)\left(1-\frac{K}{2}\right)+\cos(\beta)\cdot\sqrt{K\left(1-\frac{K}{4}\right)}\right] & e^{-\alpha}\left[\cos(\beta)\left(1-\frac{K}{2}\right)+\sin(\beta)\cdot\sqrt{K\left(1-\frac{K}{4}\right)}\right] & e^{-\alpha}\left[-\sin(\beta)\left(1-\frac{K}{2}\right)+\cos(\beta)\cdot\sqrt{K\left(1-\frac{K}{4}\right)}\right] \end{bmatrix} \begin{pmatrix} A_1 \\ A_2 \\ A_3 \\ A_4 \end{pmatrix} = \begin{pmatrix} 1 \\ \nu \\ 0 \\ 0 \end{pmatrix}$$

Where $\alpha = \pi\phi\sqrt{1-K/4}$, $\beta = \pi\phi\sqrt{K/4}$

References

Y. Aminanda, B. Castanie, J.-J. Barrau and P. Thevenet, Experimental Analysis and Modeling of the Crushing of Honeycomb Cores. Applied Composite Materials Vol 12 pp.213–227 (2005)

F. Bloom, D. Coffin, Handbook of thin plates buckling and postbuckling, Chapman & Hall/CRC (2001)

P. S. Bulson, The stability of flat plates, Elsevier (1969)

F. Cote, V.S. Deshpande, N.A. Fleck, A.G. Evans. The out-of-plane compressive behavior of metallic honeycombs. Mater. Sci. Engrg. A 380, 272–280 (2004)

F. Côté, V.S. Deshpande, N.A. Fleck, A.G. Evans. The compressive and shear responses of corrugated and diamond lattice materials. International Journal of Solids and Structures 43 pp.6220–6242 (2006)

Doyoyo M., Mohr D., Microstructural response of aluminum honeycomb to combined out-of-plane loading, Mechanics of Materials, 35, 9, 865-876, (2003).

HexWeb® Honeycomb Attributes and Properties, Hexcel Corporation (1999)

S. Kelsey, R. A. Gellatly and B. W. Clark, Foil honeycomb cores, a theoretical and experimental investigation on cores used in sandwich construction, Aircraft Engineering 30, 294-302 (1958)

R. K. Mc Farland, Hexagonal cell structures under post-buckling axial load, AIAA Journal 1, 1380-1385 (1963)

Gibson, L. J. and Ashby, M. F. Cellular Solids: Structure and Properties. Pergamon Press. Oxford (1988)

M. Grediac, A Finite Element Study of the Transverse Shear in Honeycomb Core, Int. J. Solid Struct., vol. 30, no. 13, 1777–1788 (1993).

J. Hohe, C. Beschorner, and W. Becker, Effective Elastic Properties of Hexagonal and Quadrilateral Grid Structures, Compos. Struct., vol. 46, pp. 73–89 (1999).

G.J. McShane, D.D. Radford, V.S. Deshpande, N.A. Fleck. The response of clamped sandwich plates with lattice cores subjected to shock loading. European Journal of Mechanics A/Solids 25 pp.215–229 (2006)

Mohr D., Doyoyo M., Experimental investigation on the plasticity of hexagonal aluminum honeycomb, Journal of Applied Mechanics, 71,3, 375-385 (2004)

Mohr D., Doyoyo M., Nucleation and propagation of plastic collapse bands in metallic honeycombs, Journal of Applied Physics, 94,4,2262-2270 (2003)

S.D. Papka, S. Kyriakides, In-plane compressive response and crushing of honeycomb, J. Mech. PhJs. Solids, Vol. 42, No. 10, pp. 1499-1532, (1994)

P. Qiao, J. Wang, Transverse Shear Stiffness of Composite Honeycomb Cores and Efficiency of Material, Mechanics of Advanced Materials and Structures, 12:159–172 (2005)

J. Salençon, Mécanique des milieux continus, Editions de l'Ecole Polytechnique (2002)

P. Suquet: Plasticité et rupture, Cours a l'Ecole Polytechnique (2002)

S. Timoshenko, S. Woinowsky-Krieger, Theory of plates and shells, 2nd edition, Ed. McGraw Hill (1959)

S. P. Timoshenko and J. M. Gere, Theory of Elastic Stability, McGraw-Hill, (1961)

T. Von Kármán, E. E. Sechler and L. H. Donnell, Strength of thin plates in compression, Trans. ASME 54, 53 (1932)

T. Wierzbicki, Crushing analysis of metal honeycomb, International Journal of Impact Engineering, Vol. 1, No. 2, pp 157-174 (1983)

Z. Xue, J.W. Hutchinson. A comparative study of impulse-resistant metallic sandwich plates. International Journal of Impact Engineering; Vol. 30 pp.1283 –1305 (2004)

Z. Xue, J.W. Hutchinson. Crush dynamics of square honeycomb sandwich cores. Int. J. Numer. Meth. Engng 2006; Vol. 65 pp.2221–2245 (2005).